http://www.aimspress.com/journal/mine

Mathematics in Engineering, 8(2): 308–339.
DOI:10.3934/mine.2026010
Received: 29 August 2025
Revised: 12 April 2026
Accepted: 12 April 2026
Published: 14 April 2026

Research article

Cancer detection via electrical impedance tomography and optimal control of elliptic PDEs

Ugur G. Abdulla* **and José H. Rodrigues**

Analysis & PDE Unit, Okinawa Institute of Science and Technology, 1919-1 Tancha, Onna-son, 904-0495, Japan

* **Correspondence:** Email: ugur.abdulla@oist.jp.

Abstract: We pursue a computational analysis of the biomedical problem on the identification of cancerous tumors at an early stage of development based on the Electrical Impedance Tomography (EIT) and optimal control of elliptic partial differential equations. Relying on the fact that the electrical conductivity of the cancerous tumor is significantly higher than that of healthy tissue, we consider an inverse EIT problem for identifying the conductivity map in the complete electrode model based on m current-to-voltage measurements on the boundary electrodes. A variational formulation as a PDE-constrained optimal control problem is introduced based on the novel idea of increasing the size of the input data by adding "voltage-to-current" measurements through various permutations of the single "current-to-voltage" measurement. The idea of permutation preserves the size of the unknown parameters at the expense of an increase in the number of PDE constraints. We apply a gradient projection method (GPM) based on the Fréchet differentiability in Besov-Hilbert spaces. Numerical simulations of 2D and 3D model examples demonstrate the sharp increase in the resolution of the cancerous tumor by increasing the number of measurements from m to m^2.

Keywords: cancer detection; Electrical Impedance Tomography; PDE constrained optimal control; numerical analysis; gradient projection method

1. Introduction

This paper addresses the inverse Electrical Impedance Tomography (EIT) problem of detecting an unknown conductivity inside a body, based on voltage measurements on the surface when electric currents are applied through a finite set of electrodes. Let $Q \subset \mathbb{R}^n$ be an open and bounded domain, and $\sigma : Q \to \mathbb{R}$ be the conductivity map. Let $\mathbf{E} = (E_l)_{l=1}^m$, $m \in \mathbb{N}$, be a finite set of electrodes attached to the surface ∂Q, with corresponding *contact impedance* vector $\mathbf{Z} = (Z_l)_{l=1}^m \in \mathbb{R}^m$. The electric *current pattern* vector $\mathbf{I} = (I_l)_{l=1}^m \in \mathbb{R}^m$ is applied to the electrodes $\mathbf{E}$ and the corresponding induced *voltage*

vector $\mathbf{U} = (U_l)_{l=1}^m \in \mathbb{R}^m$ is measured. The following *conservation of charges* and *grounding conditions* are satisfied:

$$\sum_{l=1}^{m} I_l = 0 \qquad \sum_{l=1}^{m} U_l = 0.$$

The potential u inside the body Q is described by the following second-order elliptic partial differential equation and corresponding boundary conditions:

$$-\mathrm{div}(\sigma(x)\nabla u) = 0, \quad \text{in} \quad Q \tag{1.1}$$

$$\sigma(x)\frac{\partial u}{\partial \nu} = 0, \quad \text{on} \quad \partial Q - \bigcup_{l=1}^{m} E_l \tag{1.2}$$

$$u + Z_l\sigma(x)\frac{\partial u}{\partial \nu} = U_l, \quad \text{on} \quad E_l,\ l = 1, \ldots, m \tag{1.3}$$

$$\int_{E_l} \frac{\partial u}{\partial \nu} ds = I_l, \qquad l = 1, \ldots, m \tag{1.4}$$

where $\nu(x) = (\nu^i(x))_{i=1,\ldots,n}$ is the outward normal at the point $x \in \partial Q$.

Inverse EIT Problem: *Given electrode contact impedance vector* $\mathbf{Z}$*, electrode current pattern* $\mathbf{I}$ *and boundary electrode measurement* $\mathbf{U}^*$*, it is required to find electrostatic potential u and electrical conductivity map* σ *satisfying* (1.1)–(1.4) with $\mathbf{U} = \mathbf{U}^*$.

The inverse EIT problem is highly ill-posed, as it aims to identify an infinite-dimensional conductivity map using finite-dimensional "current-to-voltage" measurements on the electrodes. Recently, a new variational method was introduced in [1] based on the PDE-constrained optimal control problem in a Sobolev space setting. The novelty of the control-theoretic model lies in its adaptation to the clinical situation, where additional "voltage-to-current" measurements, based on various permutations of the single "current-to-voltage" measurement, can increase the size of the input data while keeping the size of the unknown parameters fixed. In [1], the existence of the optimal control and Fréchet differentiability in Besov-Hilbert spaces is proved, the formula for the Fréchet gradient is derived, and a gradient descent algorithm in Besov-Hilbert spaces has been developed. In [2], the convergence of the finite-difference method is proved. The main goal and novelty of this paper are to pursue computational analysis and numerical simulations of the new method in 3D model examples and develop a new two-stage algorithm for the direct medical application of the method for the identification of the cancerous tumor at an early stage of development. Theoretical development accomplished in the previous works [1, 2] is applicable in an arbitrary space dimension $N \geq 2$. However, computational analysis and numerical simulation of the method are pursued only in the 2D case in [1]. A 3D case corresponding to a real-world clinical application is computationally much more challenging than a 2D case. In general, the majority of numerical methods and reconstruction algorithms for the inverse EIT problem in the literature are dedicated to the 2D case. Therefore, in-depth computational analysis of the new method in the 3D case, and development of the novel two-stage procedure for clinical application, opens a path for direct application of the methods and software developed in this paper in medical facilities.

EIT problems have numerous applications in medicine, industry, geophysics, and materials sciences [13]. Forward EIT problem (1.1)–(1.4) for the identification of $(u, \mathbf{U})$ with given input data

$(\sigma, \mathbf{I}, \mathbf{Z})$ is referred to as *complete electrode model*. It was introduced in [25] as a physically more accurate model capable of predicting experimental data with high precision. Existence and uniqueness of solution to the complete electrode model (1.1)–(1.4) was established in [25].

Motivated by the medical applications of detecting cancerous tumors from the breast tissue and other parts of the body, the relevance of the inverse EIT problem lies in the fact that the conductivity of cancerous tissue is considerably higher than the conductivity of normal tissue [11, 20].

The inverse EIT problem belongs to the class of so-called Calderon-type ill-posed inverse problems due to the celebrated work [8], where the well-posedness of the inverse problem for the identification of σ through Dirichlet-to-Neumann or Neumann-to-Dirichlet maps for the PDE (1.1) is presented. Significant developments in Calderon's inverse problem, concerning questions of uniqueness and stability, were achieved in [16, 18, 21, 22, 26].

The difficulty in solving the inverse EIT problem lies in identifying the infinite-dimensional conductivity map σ and the finite-dimensional voltage vector U from a finite number of measurements of input data. It is important to notice that the number of input data depends on the number of electrodes, and there is no flexibility to increase its size. Alternatively, an increase in measurement sets (current patterns) could be used to identify the same conductivity map; however, the number of unknown voltages would increase accordingly. A variety of numerical methods have been developed in the attempt to solve the inverse EIT problem [3–5, 9, 10, 12, 14, 15, 19, 23, 24, 27].

The majority of the methods mentioned above and reconstruction algorithms found in the literature are dedicated to the 2D inverse EIT problem. Therefore, it is natural to expect that 2D algorithms and methods could be used in the attempt to identify anomalies in a cross-section of a 3D body. However, the 3D characteristics of the current flow may be neglected, resulting in distortions in the resulting images [7]. A similar drawback has been previously observed in [17], and a reconstruction algorithm based on the inversion of the sensitivity matrix was proposed for a simplified model in a finite right circular cylinder.

2. Notation

Throughout the text, we will use the following notation of functional spaces:

- $L_2(Q)$ will denote the Hilbert space of measurable functions on Q with inner product

$$(u, v)_{L_2(Q)} := \int_Q u(x)v(x)dx, \quad u, v \in L_2(Q).$$

- $L_\infty(Q)$ will denote the Banach space of measurable functions on Q with finite norm

$$\|u\|_{L_\infty(Q)} = \text{ess sup}_{x\in Q}|u(x)|.$$

- $H^1(Q)$ will denote the Sobolev-Hilbert space of measurable functions in Q with inner product

$$(u, v)_{H^1(Q)} := (u, v)_{L_2(Q)} + (\nabla u, \nabla v)_{L_2(Q,\mathbb{R}^n)}, \quad u, v \in H^1(Q).$$

- $H^\epsilon(Q)$, $0 < \epsilon < 1$ will denote the Besov-Hilbert space of measurable functions with inner product

$$(u, v)_{H^\epsilon(Q)} := (u, v)_{L_2(Q)} + \int_Q \int_Q \frac{(u(x) - u(y))(v(x) - v(y))}{|x - y|^{1+2\epsilon}} dxdy.$$

- $\mathbf{ba}(Q) = (L_\infty(Q))'$ is the Banach space of bounded and finitely additive signed measures on Q and the dual space of $L_\infty(Q)$ with finite norm

$$\|\phi\|_{\mathbf{ba}(Q)} = |\phi|(Q),$$

where $|\phi|(Q)$ is the total variation of ϕ and defined as $|\phi|(Q) = \sup \sum_i \phi(E_i)$, where the supremum is taken over all the partitions $\bigcup E_i$ of E into measurable subsets E_i.

- $B : H^1(Q)\times H^1(Q) \to \mathbb{R}$ will denote the bilinear form associated with the PDE (1.1) and boundary conditions (1.2)-(1.3):

$$B[u, v] = \sum_{i=1}^{n} \int_Q \sigma(x) u_{x_i} v_{x_i} dx + \sum_{l=1}^{m} \frac{1}{Z_l} \int_{E_l} uv ds, \quad u, v \in H^1(Q). \tag{2.1}$$

3. Methods

3.1. Optimal control problem

We aim to formulate an inverse EIT problem as an optimal control problem by selecting the conductivity map σ and the boundary electrode voltage vector U as control parameters. Given control vector $(\sigma, \mathbf{U})$, the state vector-potential u is identified as a Sobolev-Hilbert solution of the elliptic PDE problem (1.1)–(1.3). An optimal control framework is implemented to identify the pair $(\sigma, \mathbf{U})$ which is the best candidate to fulfill Ohm's law on the electrodes (condition (1.4)). A particular advantage of this approach is the well-posedness of the elliptic problem (1.1)–(1.3) under very general assumptions on the conductivity map σ as a consequence of the powerful Lax-Milgram theory.

For a given $v = (\sigma, \mathbf{U}) \in L_\infty(Q) \times \mathbb{R}^m$, a function $u = u(\ \cdot\ ; v) \in H^1(Q)$ is called a *solution* to the PDE problem (1.1)–(1.3) if the following identity is satisfied:

$$B[u, \eta] = \sum_{l=1}^{m} \frac{U_l}{Z_l} \int_{E_l} \eta ds, \quad \forall \eta \in H^1(Q). \tag{3.1}$$

To prove the necessary optimality condition, we introduce the adjoint state problem corresponding to (1.1)–(1.3). Given a control vector $v = (\sigma, U) \in L_\infty(Q) \times \mathbb{R}^m$, let $u = u(\ \cdot\ ; v)$ be the corresponding solution of (1.1)–(1.3). The following is the *adjoined* problem to (1.1)–(1.3).

$$-\mathrm{div}(\sigma(x)\nabla\psi) = 0, \quad \text{in} \quad Q \tag{3.2}$$

$$\sigma(x)\frac{\partial\psi}{\partial\nu} = 0, \quad \text{on} \quad \partial Q - \bigcup_{l=1}^{m} E_l \tag{3.3}$$

$$\psi + Z_l\sigma(x)\frac{\partial\psi}{\partial\nu} = 2\int_{E_l} \frac{u(s) - U_l}{Z_l} dS + 2I_l, \quad \text{on} \quad E_l, \quad l = 1, \dots, m. \tag{3.4}$$

A function $\psi = \psi(\ \cdot\ ; v) \in H^1(Q)$ is a *solution* to (3.2)-(3.4) if the following identity is verified

$$B[\psi, \eta] = \sum_{l=1}^{m} \frac{2}{Z_l} \left(\int_{E_l} \frac{u - U_l}{Z_l} ds + I_l \right) \int_{E_l} \eta ds, \quad \forall \eta \in\ H^1(Q). \tag{3.5}$$

The existence, uniqueness, and stability results for the solutions to elliptic PDE problems (1.1)–(1.3) and (3.2)–(3.4) are a consequence of Lax-Milgram theory in the Sobolev-Hilbert space $H^1(Q)$ [1].

Consider the following variational formulation of the inverse EIT Problem: Given electrode current pattern I and corresponding electrode voltage measurement vector U^*, consider the minimization of the functional

$$\mathcal{J}(v) = \sum_{l=1}^{m} \left| \int_{E_l} \frac{U_l - u}{Z_l} - I_l \right|^2 + \beta |\mathbf{U} - \mathbf{U}^*|^2, \quad \beta > 0, \tag{3.6}$$

on the control set

$$V_R = \left\{ \begin{array}{c} v = (\sigma, \mathbf{U}) \in \left(L_\infty(Q) \cap H^\epsilon(Q) \right) \times \mathbb{R}^m \Big| \\ \sum_{l=1}^{m} U_l = 0, \|\sigma\|_{L_\infty} + \|\sigma\|_{H^\epsilon} + |\mathbf{U}| \le R, \ \sigma \ge \mu > 0 \end{array} \right\}$$

where $\beta > 0$, and $u = u(\ \cdot\ ; v) \in H^1(Q)$ is the solution of (1.1)–(1.3). This optimal control problem will be referred to as Problem $\mathcal{J}$. The first term in the cost functional (3.6) represents the error for the integral form of Ohm's law on the boundary electrodes (condition (1.4)) in light of the Robin boundary condition (1.3).

It should be stressed that the variational formulation of the forward EIT Problem is a particular case of the Problem $\mathcal{J}$. If the conductivity map σ is known, we consider the optimal control problem for the minimization of the function

$$\mathcal{I}(\mathbf{U}) = \sum_{l=1}^{m} \Big| \int_{E_l} \frac{U_l - u(x)}{Z_l} ds - I_l \Big|^2 \to \inf \tag{3.7}$$

in a control set

$$W = \{ \mathbf{U} \in \mathbb{R}^m \Big| \sum_{l=1}^{m} U_l = 0 \} \tag{3.8}$$

where $u = u(\cdot; \mathbf{U}) \in H^1(Q)$ is a solution of the elliptic problem (1.1)–(1.3). Furthermore, this optimal control problem will be referred to as Problem $\mathcal{I}$. It is a convex PDE constrained optimal control problem.

The optimal control problem $\mathcal{J}$ inherits the ill-posedness of the inverse EIT problem. Following [1], we now formulate the optimal control problem, which is adapted to the situation when the size of the input data can be increased through additional measurements while keeping the size of the unknown parameters fixed. Let $\mathbf{I}^1 := \mathbf{I}$ be a current pattern input, and $\mathbf{U}^1 = (U_1, ..., U_m)$ be a corresponding boundary electrode voltage measurement. Consider $m - 1$ new permutations of boundary voltages

$$\mathbf{U}^j = (U_j, \ldots, U_m, U_1, \ldots, U_{j-1}), \quad j = 2, \ldots, m, \tag{3.9}$$

of $\mathbf{U}$. The set of permutations above will be referred to as "rotation scheme". Assume that the "voltage-to-current" measurement allows us to measure associated current $\mathbf{I}^j = (I_1^j, ..., I_m^j)$, $j = 1, \ldots, m$. By setting $\mathbf{U}^1 = \mathbf{U}^*$ and having a new set of m^2 input data $\{\mathbf{I}^j\}_{j=1}^m$, we now consider an optimal control problem on the minimization of the new cost functional

$$\mathcal{K}(v) = \sum_{j=1}^{m} \sum_{l=1}^{m} \left| \int_{E_l} \frac{U_l^j - u^j}{Z_l} dS - I_l^j \right|^2 + \beta |\mathbf{U} - \mathbf{U}^*|^2, \tag{3.10}$$

on a control set V_R, where $u^j = u(\ \cdot\ ; \sigma, \mathbf{U}^j)$ is the corresponding solution to the problem (1.1)–(1.3) with U replaced by its permutation $\mathbf{U}^j$, for $j = 1, \dots, m$. This optimal control problem will be referred to as Problem $\mathcal{K}$. Note that the number of input currents in the Problem $\mathcal{K}$ has increased from m to m^2. However, the size of the unknown control vector is unchanged, and in particular, there are only m unknown voltages $U_1, \cdots, U_m$, whereas all vectors $\mathbf{U}^j$, $j = 2, ..., m$ are formed by their permutation as in (3.9). The price we pay for this gain is the increase in the number of PDE constraints from 1 to m. It is essential to note that the Problem $\mathcal{J}$ is a particular case of the Problem $\mathcal{K}$, precisely when we don't consider any permutation of $\mathbf{U}^1$, but the trivial one.

Remark 3.1. Note that the conductivity component of the control variable is sought within the L_∞-class of functions in the domain Q, rather than being restricted to piecewise constant functions. This choice enables broad applicability, allowing the target conductivity to be characterized by multiple levels corresponding to different properties or measurements of tissue. For the numerical simulations presented in Section 4, we distinguish healthy from tumorous tissue only, reflecting real experimental data.

3.2. Fréchet differentiability

Existence of an optimal control for the problem $\mathcal{K}$ (consequently $\mathcal{J}$) and Fréchet differentiability was proved in [1]. In [2], the convergence of the method of finite differences is established.

Theorem 3.2 (Fréchet differentiability)**.** *[1] The functional $\mathcal{K}$ is differentiable on V_R in the sense of Fréchet and the corresponding Fréchet gradient $\mathcal{K}' : V_R \to \boldsymbol{ba}(Q) \times \mathbb{R}^m$ is given by $\mathcal{K}'(v) = \left(\mathcal{K}'_\sigma(\sigma, \mathbf{U}), \mathcal{K}'_\mathbf{U}(\sigma, \mathbf{U})\right)$ where*

$$\mathcal{K}'_\sigma(\sigma, \mathbf{U}) = -\sum_{j=1}^{m} \nabla\psi^j \cdot \nabla u^j, \tag{3.11}$$

$$\mathcal{K}'_\mathbf{U}(\sigma, \mathbf{U}) = \left(\sum_{j,l=1}^{m} 2\left[\int_{E_l} \frac{U_l^j - u^j(s)}{Z_l} dS - I_l^j \right] \int_{E_l} \frac{\delta_{l\theta_{kj}} - w^{\theta_{kj}}(s)}{Z_l} dS + 2\beta(U_k - U_k^*) \right)_{k=1}^{m}, \tag{3.12}$$

where

$$\theta_{kj} = \begin{cases} k - j + 1, & \text{if } j \le k, \\ m + k - j + 1, & \text{if } j > k, \end{cases} \tag{3.13}$$

and $w^{\theta_{kj}} = u(\ \cdot\ ; \sigma, e_{\theta_{kj}})$ and $e_{\theta_{kj}} \in \mathbb{R}^m$ is the unit vector in the θ_{kj}-direction.

3.3. Gradient method in Besov-Hilbert space

Fréchet differentiability result suggests the following algorithm based on the projective gradient method for the Problem $\mathcal{K}$.

Step 1. Set iteration counter $N = 0$ and choose initial controls $v^N = (\sigma_N, \mathbf{U}^N) \in V_R$, where $\mathbf{U}^N = (U_l^N)_{l=1}^m$ satisfies $\sum_{l=1}^m U_l^N = 0$.

Step 2. Build the pertmutations $\mathbf{U}^{N,j}$, solve the problem (1.1)–(1.3) to find $u^{N,j} = u(\ \cdot\ ; \sigma_N, \mathbf{U}^{N,j})$, $j = 1, \dots, m$, and calculate $\mathcal{K}^N = \mathcal{K}(\sigma_N, \mathbf{U}^N)$.

Step 3. If $N = 0$, move to Step 4. Otherwise, check for the error condition

$$\max\left(\left|\frac{\mathcal{K}^N - \mathcal{K}^{N-1}}{\mathcal{K}^{N-1}}\right|, \frac{|\mathbf{U}^N - \mathbf{U}^{N-1}|}{|\mathbf{U}^{N-1}|}, \frac{\|\sigma_N - \sigma_{N-1}\|_{L_2}}{\|\sigma_{N-1}\|_{L_2}}\right) < \epsilon_{tol}, \tag{3.14}$$

where $\epsilon_{tol} > 0$ is the required relative error tolerance. If (3.14) is verified, then terminate the iteration process. Otherwise, move to Step 4.

Step 4. Solve the problem (1.1)–(1.3) to find $w_k^N = u(\,\cdot\,; \sigma_N; e_k)$, where $e_k \in \mathbb{R}^m$ is the unit vector in the k-direction, $k = 1, \ldots, m$.

Step 5. Solve the adjoined problem (3.2)–(3.4) to find adjoined potential $\psi^{N,j} = \psi(\,\cdot\,; \sigma_N, \mathbf{U}^{N,j}, u^{N,j})$, for $j = 1, \ldots, m$.

Step 6. Choose step size parameter $\gamma^N > 0$ and compute new control vector $v^{N+1} = (\sigma_{N+1}, \mathbf{U}^{N+1})$ using the Fréchet differentiability expressions (3.11) and (3.12) as follows:

$$\sigma_{N+1}(x) = \sigma_N(x) + \gamma^N \sum_{j=1}^{m} \nabla\psi^{N,j}(x) \cdot \nabla u^{N,j}(x), \quad x \in Q, \tag{3.15}$$

$$U_k^{N+1} = U_k^{N+1} - \gamma^N \left[\sum_{j,l=1}^{m} 2\left(\int_{E_l} \frac{U_l^{N,j} - u^{N,j}}{Z_l} dS\right) \int_{E_l} \frac{\delta_{l,\theta_{kj}} - w^{\theta_{kj}}}{Z_l} dS + 2\beta(U_k^N - U_k^*)\right], \tag{3.16}$$

for $k = 1, \ldots, m$.

Step 7. Update new control susing the following projection formulas $\sigma_{N+1} = \text{proj}(\sigma_{N+1})$ and $\mathbf{U}^{N+1} = \text{proj}(\mathbf{U}^{N+1})$ given by

$$\text{proj}(\sigma_{N+1})(x) = \begin{cases} \mu, & \text{if} \quad \sigma_{N+1}(x) \le \mu, \\ \sigma_{N+1}(x), & \text{if} \quad \mu \le \sigma_{N+1}(x) \le R, \\ R, & \text{if} \quad \sigma_{N+1}(x) \ge R, \end{cases}, \quad x \in Q, \tag{3.17}$$

$$\text{proj}(\mathbf{U}^{N+1})_k = U_k^{N+1} - \frac{1}{m}\sum_{l=1}^{m} U_l^{N+1}, \quad k = 1, \ldots, m. \tag{3.18}$$

Then, replace N by $N + 1$ and move to Step 2.

3.4. Three-stage procedure for simulations and clinical applications

The above algorithm suggests the following two-stage procedure, with the increase of data, both in simulations and in clinical applications.

- *Simulation-Stage 1*: Select one set of electrode current input $\mathbf{I}^1 = (I_l^1)_{l=1}^m$ and the conductivity map σ_{true} reflecting a distribution of cancerous tumor. Solve the convex optimization Problem $\mathcal{I}$ and find its unique minimizer $\mathbf{U}^{true}$. Let $\mathbf{U}^* = \mathbf{U}^{true}$. The pair $(\sigma_{true}, u_{true})$ is the solution of the inverse EIT problem with input data $(\mathbf{Z}, \mathbf{I}^1, \mathbf{U}^*)$. Here, $u_{true} = u(\cdot; \sigma_{true}, \mathbf{U}^*)$ is the solution of the elliptic PDE problem (1.1)–(1.3).
- *Simulation-Stage 2*: Solve the optimal control problem $\mathcal{J}$ with a single set of m input data $\mathbf{I}^1 = (I_l^1)_{l=1}^m$ by the GPM algorithm to recover $(\sigma_{true}, \mathbf{U}^{true})$.

- *Simulation-Stage 3*: Denote $\mathbf{U}^1 = \mathbf{U}^*$ and consider $m-1$ permutations $\{\mathbf{U}^j\}_{j=2}^m$ as in (3.9). Denote $u^1 \equiv u_{true}$, and for each $j = 2, ..., m$, solve the elliptic PDE problem (1.1)–(1.3) to find functions $u^j = u(\cdot; \sigma_{true}, \mathbf{U}^j)$. Then use the "voltage-to-current" formula (1.4) with $u = u^j$ to calculate $m-1$ new sets of current vectors $\mathbf{I}^j$, $j = 2, ..., m$. This procedure guarantees that $(\sigma_{true}, \mathbf{U}^{true})$ is an optimal control for the Problem $\mathcal{K}$. Solve the optimal control Problem $\mathcal{K}$ with m^2 input data $\{I_l^j\}_{j,l=1,...,m}$ by the GPM algorithm to recover an optimal control $(\sigma_{true}, \mathbf{U}^{true})$.

Our main results suggest the following two-stage procedure for medical application for the identification of the cancerous tumor at an early stage of development:

- *Clinical Application-Step 1*: Apply selected one set of electrode current vector $\mathbf{I}^1 = (I_l^1)_{l=1}^m$ on the electrodes $\mathbf{E} = (E_l)_{l=1}^m$, take the "current-to-voltage" measurements $\mathbf{U}^1 = (U_l^1)_{l=1}^m$.

- *Clinical Application-Step 2*: Consider $m-1$ permutations $\{\mathbf{U}^j\}_{j=2}^m$ as in (3.9); apply each voltage vector U^j to electrodes; pursue "voltage-to-current" measurements $\mathbf{I}^j = (I_l^j)_{l=1}^m$, and then solve the optimal control Problem $\mathcal{K}$ with m^2 input data $\{I_l^j\}_{j,l=1,...,m}$ by the GPM algorithm to identify the location of development of the cancerous tumor.

4. Numerical results

4.1. Methodology

4.1.1. Finite element approach

The PDE problem (1.1)–(1.3) and its adjoint (3.2)–(3.4) are numerically solved using the *partial differential equation toolbox* package of Matlab. This package applies a linear *finite element* spatial discretization $\mathcal{T}_Q = \bigcup T^e$ of the domain Q, where T^e is a finite element (triangle in 2D or tetrahedron in 3D). If $\{\phi_i\}_{i=1,...,N_d}$ denotes the piecewise polynomial basis of functions, where N_d is the number of nodes in the discretization, then the approximate solution of problem (1.1)–(1.3) is written as $u_{\text{fem}} = \sum_{i=1}^{N_d} u^i \phi_i$ where u^i is the undetermined scalar corresponding to the potential u at the node i. Hence, the variational formulation yields the linear system

$$\sum_{i=1}^{N_d} u^i \left[\int_{T^e} \sigma \nabla \phi_i \cdot \nabla \phi_j dx + \sum_{l=1}^{m} \frac{1}{Z_l} \int_{\partial T^e \cap E_l} \phi_i \phi_j dS \right] = \sum_{l=1}^{m} \frac{U_l}{Z_l} \int_{\partial T^e \cap E_l} \phi_j dS, \tag{4.1}$$

for $j = 1, \ldots, N_d$. Analogously, if $\psi_{\text{fem}} = \sum_{i=1}^{N_d} \psi^i \phi_i$ corresponds to the discretization of the adjoined potential ψ, then the corresponding variational formulation yields

$$\begin{aligned} &\sum_{i=1}^{N_d} \psi^i \left[\int_{T^e} \sigma \nabla \phi_i \cdot \nabla \phi_j dx + \sum_{l=1}^{m} \frac{1}{Z_l} \int_{\partial T^e \cap E_l} \phi_i \phi_j dS \right] \\ &= \sum_{l=1}^{m} \int_{\partial T^e \cap E_l} \frac{\phi_j}{Z_l} \left[2 \int_{\partial T^e \cap E_l} \frac{u_{\text{fem}} - U_l}{Z_l} dS + 2 I_l \right] dS, \end{aligned} \tag{4.2}$$

for $j = 1, \ldots, N_d$.

For the inverse EIT problem, we start by setting the current I and contact impedance Z vectors as described in the previous section. To simulate the EIT model, we set the conductivity map $\sigma_{true} : Q \to \mathbb{R}$ to emulate spherical tumor regions of center c and radius $r > 0$ inside Q, namely

$$\sigma_{true}(x) = \begin{cases} 0.4, & \text{if } |x - c| \leq r; \\ 0.2, & \text{otherwise,} \end{cases} \qquad \text{in } (\text{Ohm} \cdot \text{m})^{-1}. \tag{4.3}$$

4.1.2. Choice of learning rate parameter γ

For all the simulations, the learning rate parameter γ^N in Step 6 of the GPM algorithm described in Section 3.3 was calculated in each iteration as the average of Barzilai-Borwein-type formulas [6]. Indeed, separate coefficients were calculated for each variable (voltage and conductivity) as follows:

$$\begin{aligned} \gamma_U^N &= \text{mean}\left(\frac{|dU^N|^2}{|dU^N \cdot d\mathcal{K}'^N_U|} \, , \, \frac{|dU^N \cdot d\mathcal{K}'^N_U|}{|d\mathcal{K}'^N_U|^2} \right), \\ \gamma_\sigma^N &= \text{mean}\left(\frac{\|d\sigma_N\|^2_{L_2}}{(d\sigma_N, d\mathcal{K}'^N_\sigma)_{L_2}} \, , \, \frac{(d\sigma_N, d\mathcal{K}'^N_\sigma)_{L_2}}{\|d\mathcal{K}'^N_\sigma\|^2_{L_2}} \right), \end{aligned} \tag{4.4}$$

where

$$\begin{aligned} dU^N &= \mathbf{U}^N - \mathbf{U}^{N-1}, \quad d\mathcal{K}'^N_U = \mathcal{K}'_{\mathbf{U}}(\sigma_N, \mathbf{U}^N) - \mathcal{K}'_{\mathbf{U}}(\sigma_{N-1}, \mathbf{U}^{N-1}), \\ d\sigma_N &= \sigma_N - \sigma_{N-1}, \quad d\mathcal{K}'^N_\sigma = \mathcal{K}'_\sigma(\sigma_N, \mathbf{U}^N) - \mathcal{K}'_\sigma(\sigma_{N-1}, \mathbf{U}^{N-1}). \end{aligned}$$

4.1.3. Tumor resolution error

To measure the approximation error of the reconstructed conductivity in the tumor region ($\mathfrak{T}$), we consider a finite element discretization $\mathcal{T}_Q$ of the domain Q and restrict the L_2 norm to the finite elements T (triangles in 2D or tetrahedrons in 3D) that are contained in the tumor region $\mathfrak{T}$. Therefore, if σ_{true} is the true conductivity and σ_{end} is the obtained conductivity at the last iteration of the GPM algorithm, then we define the *tumor resolution error* (TRE) by

$$\text{TRE}(\sigma_{end}) = \left\{ \sum_{T^e \in \mathcal{T}_Q \cap \mathfrak{T}} \int_{T^e} |\sigma_{true}(x) - \sigma_{end}(x)|^2 dx \right\}^{1/2}. \tag{4.5}$$

Since the values of the conductivity σ_{true} (resp. σ_{end}) are known only at the vertices of each finite element T^e, we denote σ^e_{true} (resp. σ^e_{end}) the mean value of σ_{true} (resp. σ_{end}) on the vertices of T^e. Note that $\sigma^e_{true} = 0.4$ for every $T^e \in \mathcal{T}_Q \cap \mathfrak{T}$. Therefore, expression (4.5) is approximated by

$$\text{TRE}(\sigma_{end}) \approx \left\{ \sum_{T^e \in \mathcal{T}_Q \cap \mathfrak{T}} |T^e| |0.4 - \sigma^e_{end}|^2 \right\}^{1/2}, \tag{4.6}$$

where $|T^e|$ denotes the measure (area in 2D or volume in 3D) of the finite element T^e. The percentage of accuracy in the tumor region (PAT) $\mathfrak{T}$ is therefore given by

$$\text{PAT}(\sigma_{end}) = \left(1 - \frac{\text{TRE}(\sigma_{true}, \sigma_{end})}{C(\mathcal{T}_Q, \mathfrak{T})} \right) \times 100, \tag{4.7}$$

where $C(\mathcal{T}_Q, \mathfrak{T})$ is the maximum error in the tumor region, given by

$$C(\mathcal{T}_Q, \mathfrak{T}) = 0.2 \left\{ \sum_{T^e \in \mathcal{T}_Q \cap \mathfrak{T}} |T^e| \right\}^{1/2}. \tag{4.8}$$

4.2. Results in 2D

In this case, we set Q to be the circle of radius $r = 0.1$m given by

$$Q = \left\{ (x, y) \in \mathbb{R}^2 : \ x^2 + y^2 < r^2 \right\}.$$

A set of $m = 16$ electrodes with dimension 0.024 rad width were uniformly distributed along the boundary ∂Q, see Figure 1(a). A mesh consisting of 2034 nodes and 3794 linear elements (triangles) was considered. A uniform contact impedance vector $\mathbf{Z} = (Z_l)_{l=1,\dots,16}$ with $Z_l = 0.1$ Ohm was set. Background conductivity is set to 0.2 $(\text{Ohm} \cdot \text{m})^{-1}$ corresponding to healthy tissue, while tumorous tissue corresponds to 0.4 $(\text{Ohm} \cdot \text{m})^{-1}$. The current vector $\mathbf{I}$ is set as shown in Figure 1(b).

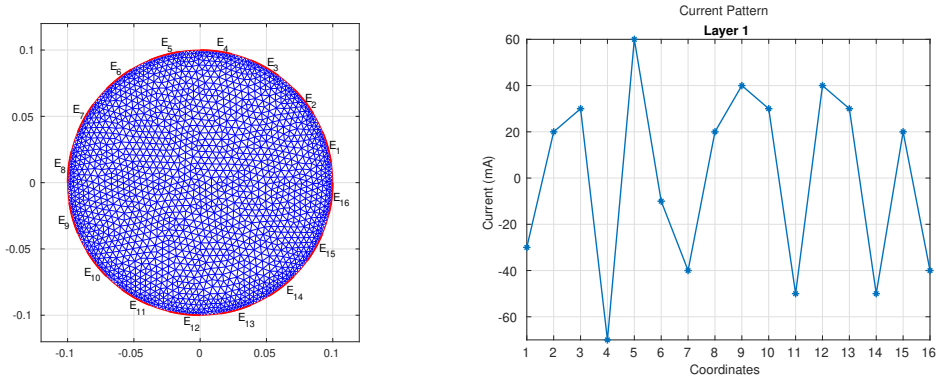

(a) Domain Q. **(b)** Current pattern.

Figure 1. (a) Meshed domain Q and electrodes position. (b) Current pattern used for all cases.

For the optimization process using the GPM algorithm described in Section 3.3, we set initial conductivity map $\sigma_{ini} = 0.3$ $(\text{Ohm} \cdot \text{m})^{-1}$ and initial voltage vector $\mathbf{U}^{ini} = (U_l^{ini})_{l=1,\dots,m}$ as follows: $U_l^{ini} = 1$ volt if l is even, $U_l^{ini} = -1$ volt if l is odd. Termination conditions for the GPM were set to a maximum number of iterations $N_{max} = 250$ or relative error tolerance $\epsilon_{tol} = 10^{-6}$. Finally, the following notation for the relative error (RE) of voltage and conductivity, respectively, will be used

$$\text{RE}(\mathbf{U}^1, \mathbf{U}^2) = \frac{|\mathbf{U}^1 - \mathbf{U}^2|}{|\mathbf{U}^2|}; \quad \text{RE}(\sigma_1, \sigma_2) = \frac{\|\sigma_1 - \sigma_2\|_{L_2}}{\|\sigma_2\|_{L_2}}.$$

4.2.1. Case: 1 tumor

We first consider the case of σ_{true} with center $c = (0, -0.05)$ and radius $r = 0.03$ see Figure 2(a). An optimal control framework is implemented without regularization ($\beta = 0$). Figure 2(b,c) shows the

contour plot of σ_N obtained for Stage 2 at final iteration $N = 33$, and Stage 3 at final iteration $N = 250$, respectively. Dashed black lines show the position and size of the target σ_{true}.

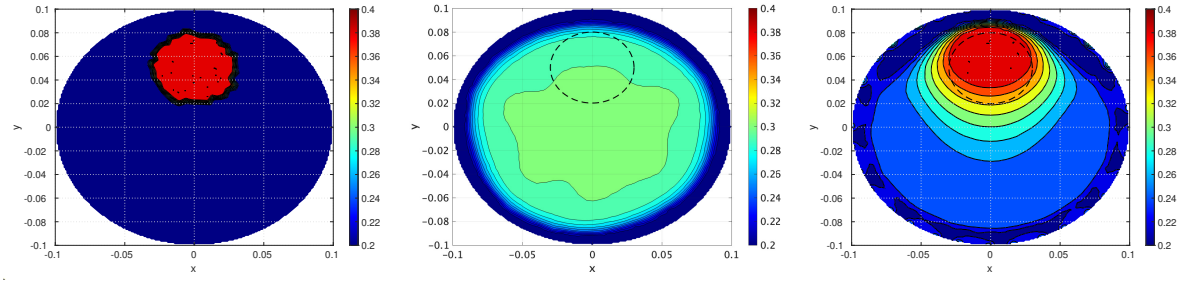

(a) σ_{true} **(b)** σ_{33} for Stage 2. **(c)** σ_{250} for Stage 3.

Figure 2. Contour plots of true and obtained conductivities for Stages 2 and 3 at the last iteration.

Figure 3 shows the coordinates of optimal voltage $\mathbf{U}^*$, initial voltage $\mathbf{U}^{ini}$, and obtained voltage $\mathbf{U}^N$ at the last iteration $N = 250$ of Stage 3, and the values of the corresponding cost functional $\mathcal{K}(\sigma_N, \mathbf{U}^N)$. Cost value at the final iteration of Stage 3 is $\mathcal{K}(\sigma_{250}, \mathbf{U}^{250}) = 5.2984\text{e-}07$, and the corresponding relative error of voltage and conductivity are, respectively, $\mathrm{RE}(\mathbf{U}^{250}, \mathbf{U}^*) = 0.0787$ and $\mathrm{RE}(\sigma_{250}, \sigma_{true}) = 0.2757$. In addition, the tumor resolution error is $\mathrm{TRE}(\sigma_{250}) = 8.1108\text{e-}04$ and the percentage of accuracy in the tumor region is $\mathrm{PAT}(\sigma_{250}) = 91.67\%$. The corresponding quantities updated for Stage 2 are as follows: $\mathcal{K}(\sigma_{33}, \mathbf{U}^{33}) = 3.1588\text{e-}25$, $\mathrm{RE}(\mathbf{U}^{33}, \mathbf{U}^*) = 0.0861$, $\mathrm{RE}(\sigma_{33}, \sigma_{true}) = 0.3642$, $\mathrm{TRE}(\sigma_{33}) = 4.9151\text{e-}03$ and $\mathrm{PAT}(\sigma_{33}) = 49.53\%$.

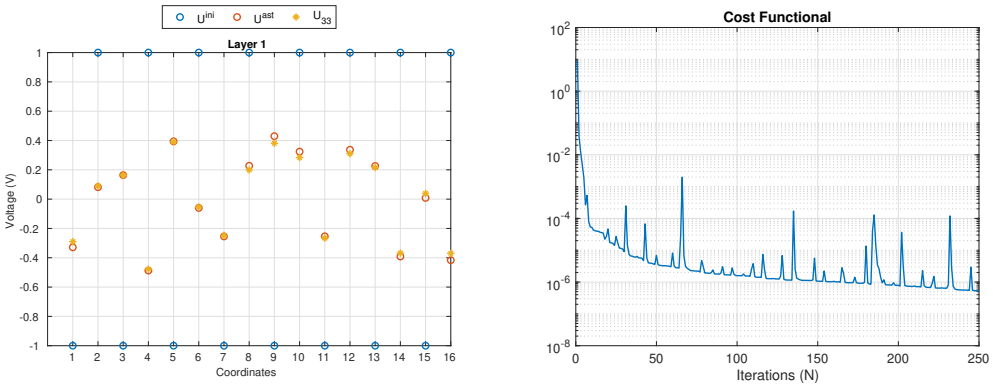

(a) U_l^{250} for Stage 3. **(b)** $\mathcal{K}(\sigma_N, \mathbf{U}^N)$ for Stage 3.

Figure 3. Voltage coordinates U_l^{250}, $l = 1, \ldots, 16$, corresponding to the first layer of electrodes, at the last iteration at Stage 3, and corresponding cost functional.

Remark 4.1. The results of Stage 2 indicate that the considered tumorous region is not identified, despite the cost functional attaining relatively small values. In contrast, the results of Stage 3 demonstrate a substantial improvement in both resolution and identification of the conductivity map when the amount of input data is increased from m to m^2 by employing the "rotation scheme".

Sensitivity with respect to size. To demonstrate the sensitivity of the method and calculations, we

fix the position c of σ_{true} and consider different values of radius, namely $r = 0.025, 0.020, 0.015, 0.010, 0.005$. Figure 4 shows the reconstructed conductivity σ_N, at iteration $N = 250$, for case $r = 0.25, 0.20, 0.15$. Dashed lines show the position and size of σ_{true}. Table 1 shows the cost values and relative error of voltage and conductivity, as well as the tumor resolution error and percentage of accuracy in the tumor region at the last iteration of Stage 3 for each case of radius r.

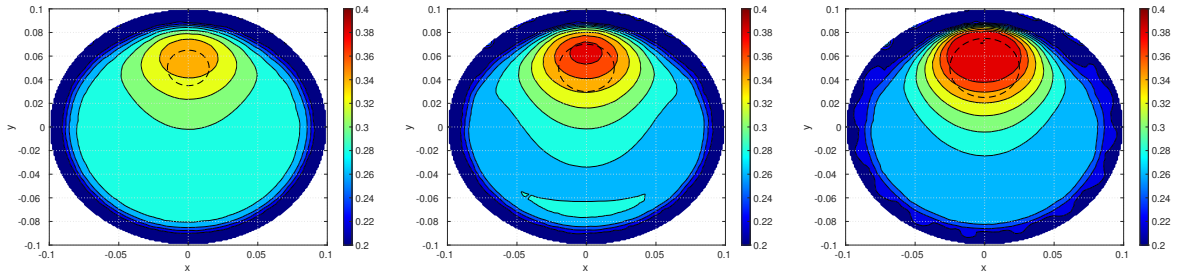

(a) $r = 0.015$ **(b)** $r = 0.020$ **(c)** $r = 0.025$

Figure 4. Contour plot of obtained conductivity σ_{250} for different values of radius r of true conductivity. Dashed lines represent the size and position of true conductivity.

Table 1. Metrics for the 2D - Case 1 tumor - Size.

Radius	Cost value	Relative error		TRE(σ_{end})	PAT(σ_{end})
(r)	$\mathcal{K}(\sigma_{end}, \mathbf{U}^{end})$	RE($\mathbf{U}^{end}, \mathbf{U}^*$)	RE($\sigma_{end}, \sigma_{true}$)		
0.030	5.2984e-07	0.0787	0.2757	8.1108e-04	91.67%
0.025	3.2890e-07	0.0830	0.3406	6.4833e-04	91.78%
0.020	1.6377e-07	0.0874	0.3642	1.0006e-03	83.88%
0.015	6.6754e-08	0.0917	0.3907	1.1599e-03	73.45%
0.010	8.8539e-09	0.0946	0.4051	9.2128e-04	62.57%
0.005	7.2273e-10	0.0960	0.4110	3.4303e-04	54.34%

Sensitivity with respect to position. For this analysis, we fixed the radius r of σ_{true} and considered different positions of center $c = (0, c_y)$, $c_y = 0.05, 0.04, 0.03, 0.02, 0.01$. Figure 5 shows the reconstructed conductivity σ_N at iteration $N = 250$ for cases $c_y = 0.04, 0.03, 0.02$. Dashed lines show the location of σ_{true}. Table 2 shows the cost value and relative error of voltage and conductivity at the last iteration for each case of center c.

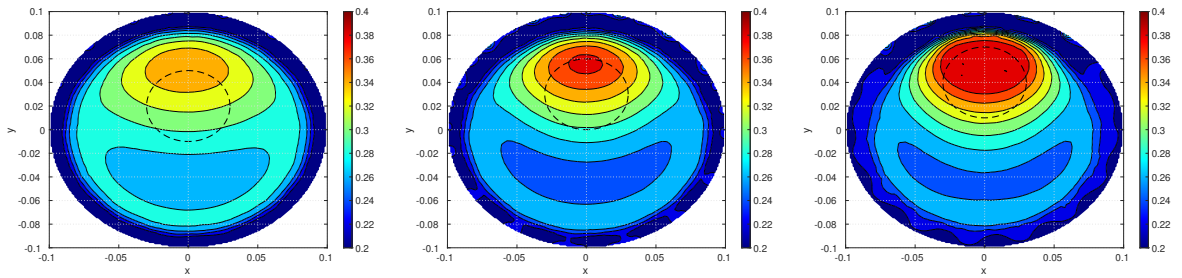

(a) $c = (0, 0.02)$ **(b)** $c = (0, 0.03)$ **(c)** $c = (0, 0.04)$

Figure 5. Contour plot of obtained conductivity σ_{250} for different values of center c of true conductivity. Dashed lines represent the size and position of true conductivity.

Table 2. Metrics for the 2D - Case 1 tumor - Location.

Center	Cost value	Relative error		TRE(σ_{end})	PAT(σ_{end})
(c_y)	$\mathcal{K}(\sigma_{end}, \mathbf{U}^{end})$	RE($\mathbf{U}^{end}, \mathbf{U}^*$)	RE($\sigma_{end}, \sigma_{true}$)		
0.05	5.2984e-07	0.0787	0.2757	8.1108e-04	91.67%
0.04	3.9891e-07	0.0776	0.3119	1.2559e-03	87.13%
0.03	1.7854e-07	0.0797	0.3089	2.7827e-03	71.27%
0.02	1.1384e-07	0.0791	0.3480	3.7884e-03	61.28%
0.01	2.7750e-08	0.0795	0.3582	4.5531e-03	53.17%
0.00	6.0320e-11	0.0794	0.3615	4.8376e-03	50.23%

4.2.2. Case: 4 tumors

We consider here σ_{true} describing 4 circular tumor regions given by centers $c_1 = (0, 0.050)$, $c_2 = (0.025, -0.055)$, $c_3 = (-0.015, -0.020)$, $c_4 = (-0.075, -0.010)$, and corresponding radius $r_1 = 0.03$, $r_2 = 0.0235$, $r_3 = 0.0122$ and $r_4 = 0.0063$. The contour plot of the true conductivity σ_{true} and reconstructed conductivity for Stage 3 after $N = 250$ iterations is shown in Figure 6. The cost value at the final iteration of Stage 3 is $\mathcal{K}(\sigma_{250}, \mathbf{U}^{250}) = 5.5801\text{e-}07$ and the corresponding relative errors of voltage and conductivity are RE($\mathbf{U}^{250}, \mathbf{U}^*$) = 0.0610 and RE($\sigma_{250}, \sigma_{true}$) = 0.2552, respectively. Tumore resolution error is TRE(σ_{250}) = 3.1500e-03 and percentage of accuracy in the tumor region is PAT(σ_{250}) = 75.48%. The optimal control framework is implemented without regularization ($\beta = 0$).

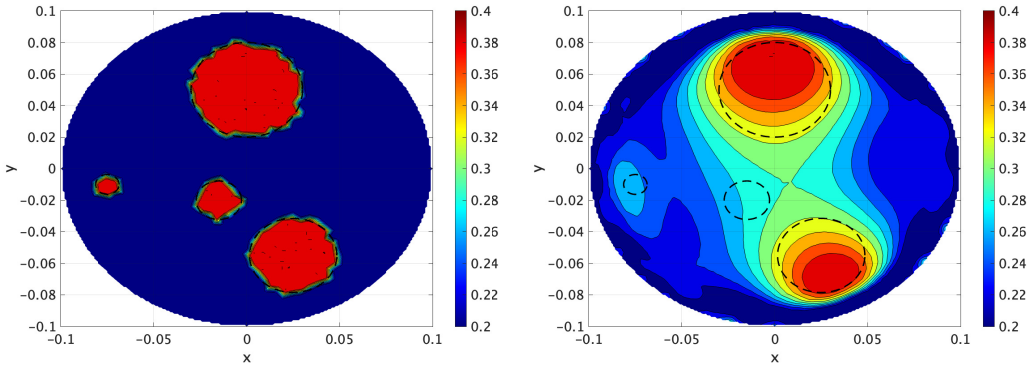

(a) σ_{true} **(b)** σ_{250} for Stage 3

Figure 6. (a) True conductivity showing position and size of 4 tumors. (b) Contour plot of the obtained conductivity σ_{250} for Stage 3. Dashed black lines correspond to the size and position of tumor regions.

Sensitivity with respect to size. For this analysis, we considered different values of c_4 and r_4. We steadily increased the radius r_4 of the smallest tumor, while recalculating its center c_3 to preserve the distance to the boundary. Figure 7 shows the reconstructed conductivity σ_{250} for each case of radius r_4 and corresponding center c_4. The identification of the corresponding tumor cell improves as the radius r_4 increases. Table 3 shows the cost value and relative error of voltage and conductivity at the last iteration of Stage 3 for each case of radius r_4.

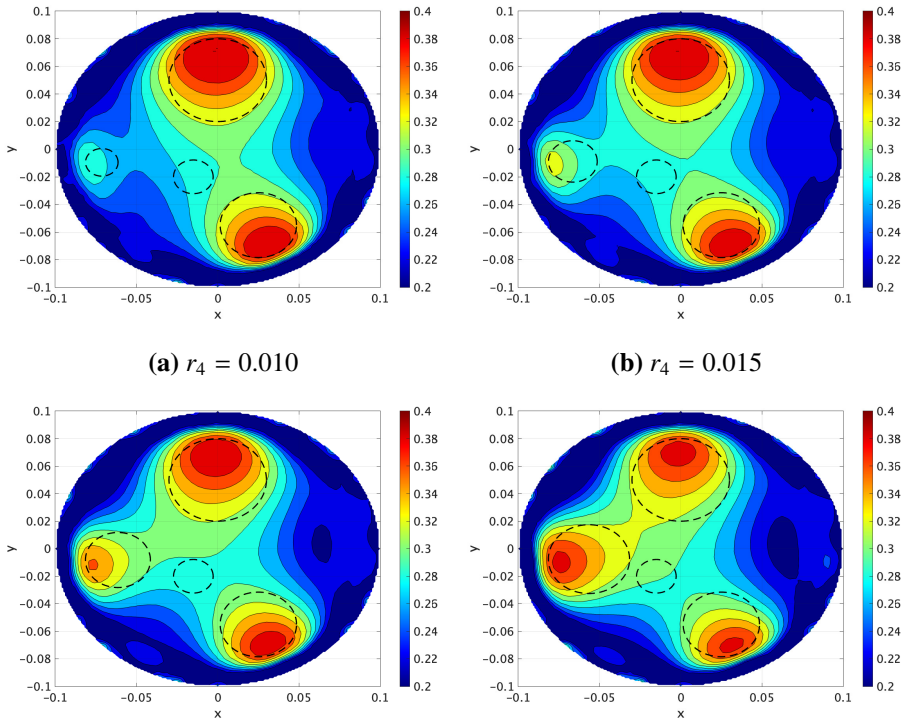

(a) $r_4 = 0.010$ **(b)** $r_4 = 0.015$

(c) $r_4 = 0.020$ **(d)** $r_4 = 0.025$

Figure 7. Contour plot of obtained conductivity σ_{250} for different values of radius r_4 in Stage 3. Dashed lines represent the size and location of each tumor of true conductivity.

Table 3. Metrics for the 2D - Case 4 tumor - Size.

Radius	Cost value	Relative error		TRE(σ_{end})	PAT(σ_{end})
(r_4)	$\mathcal{K}(\sigma_{end}, \mathbf{U}^{end})$	RE($\mathbf{U}^{end}, \mathbf{U}^*$)	RE($\sigma_{end}, \sigma_{true}$)		
0.0100	7.2617e-07	0.0602	0.2624	3.4712e-03	73.32%
0.0150	6.5505e-07	0.0581	0.2604	3.9172e-03	70.95%
0.0200	5.1999e-07	0.0555	0.2516	4.2044e-03	70.36%
0.0250	6.4377e-07	0.0504	0.2439	4.5225e-03	70.02%

Regularization effect. Here, we consider the effect of regularization for the refinement of the resolution of the reconstructed conductivity. The cost values $\mathcal{K}(\sigma_\beta, \mathbf{U}^\beta)$, where σ_β and $\mathbf{U}^\beta$ are the corresponding conductivity and voltage coordinates at the end of 250 iterations at Stage 3 for several values of β, plotted on a logarithmic scale, are shown in Figure 8(a). The dashed line corresponds to the cost value $\mathcal{K}(\sigma_{250}, \mathbf{U}^{250})$ obtained after 250 iterations without regularization, i.e., $\beta = 0$. Figure 8(b) shows the corresponding relative errors of conductivity RE($\sigma_\beta, \sigma_{true}$) and voltage RE($\mathbf{U}^\beta, \mathbf{U}^*$). In particular, the conductivity map for a sample of values of β is displayed in Figure 9.

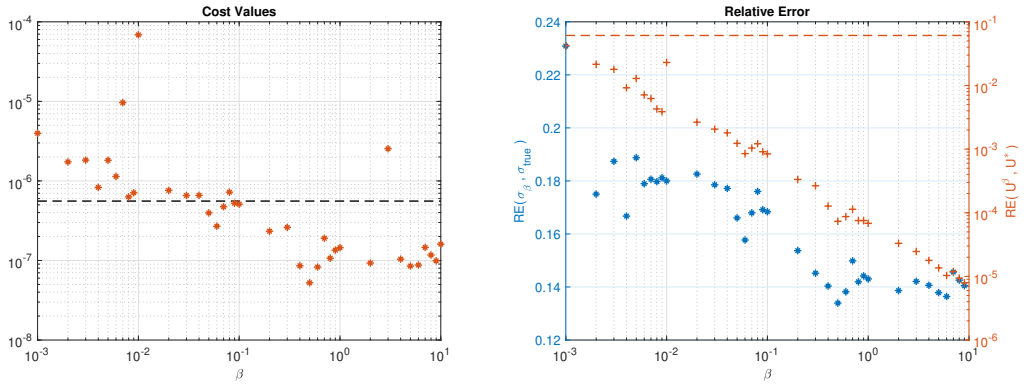

(a) Cost values. **(b)** Relative error.

Figure 8. Regularization results for several values of the parameter β in the logarithmic scale. Dashed lines correspond to the values obtained for the case $\beta = 0$.

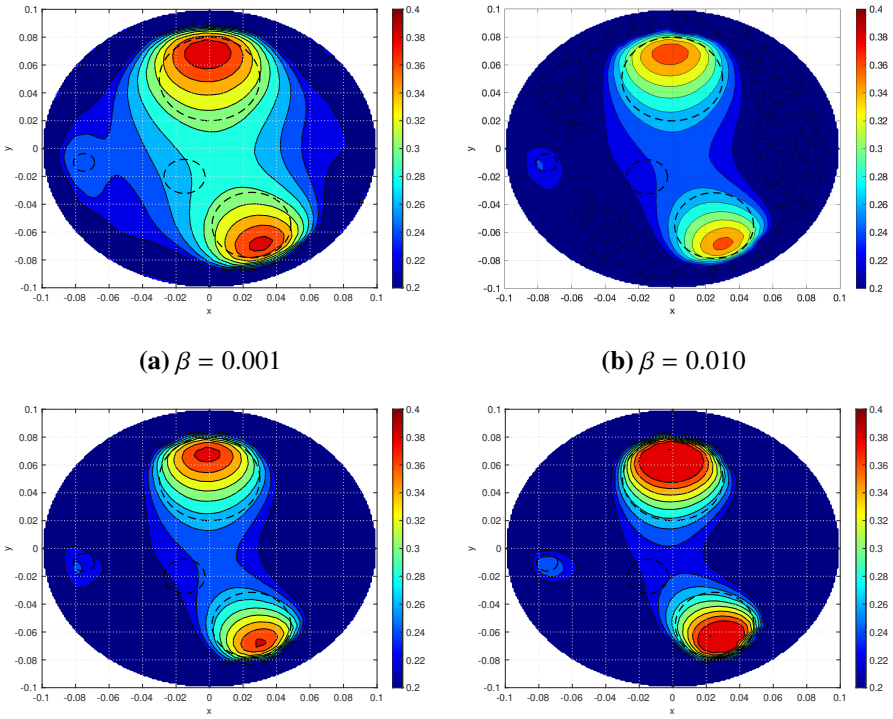

(a) $\beta = 0.001$ **(b)** $\beta = 0.010$

(c) $\beta = 0.100$ **(d)** $\beta = 1.000$

Figure 9. Stage 3 regularized conductivity σ_β for some values of β.

Based on the cost values and the relative errors obtained and displayed in the Figure 8, we select $\beta = 0.5$ and increase the number of iterations during Stage 3. The resulting conductivity map is displayed in Figure 10. In this scenario, cost value at the last iteration is $\mathcal{K}(\sigma_{1000}, \mathbf{U}^{1000}) = 9.5084\text{e-}09$, and relative errors of voltage and conductivity are $\text{RE}(\mathbf{U}^{1000}, \mathbf{U}^*) = 2.7865\text{e-}05$ and $\text{RE}(\sigma_{1000}, \sigma_{true}) = 0.1030$, respectively. In addition, the tumor resolution error is $\text{TRE}(\sigma_{1000}) = 3.2722\text{e-}03$ and the percentage of accuracy in the tumor region is $\text{PAT}(\sigma_{1000}) = 74.53\%$. Remarkably, improved cost functional minimum

and resolution error (compare to the first line of the Table 3) as a result of regularization, the resolution of the reconstructed optimal conductivity is significantly refined. Comparing Figure 10 to Figure 8(a), we see that the resolution of the reconstructed conductivity recognizes the smaller size tumors as an effect of regularization.

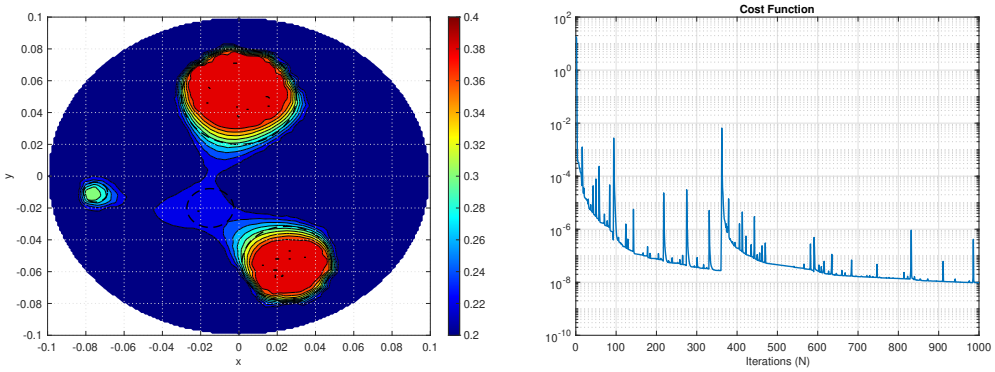

(a) Conductivity **(b)** Cost Functional

Figure 10. Conductivity map for $\beta = 0.5$ after 1000 iterations, and corresponding cost functional.

Remark 4.2. Sensitivity results show that the quality and precision of the conductivity map improve with the size of the tumorous region and its proximity to the electrodes. It is essential to note that the size of the mesh and the weakening of the electrical potential flux away from the electrodes, i.e., towards the center of the domain, may impact the results. Regarding the 4-tumors case, in particular, when considering voltage regularization effects, resolution and localization are improved as the value of the regularization parameter β increases. The particular case $\beta = 0.5$ provides the lowest cost value (among the cases considered), and the extrapolation on the number of iterations shows a relative error as low as 10%, while cost values seem to reach a threshold approximately at 9e-09. As a result, the resolution of the reconstructed conductivity is significantly improved, and smaller-sized tumors are recognized, despite being lost in the resolution of the reconstructed conductivity without regularization.

Noise effect. We consider here the case in which the measured voltage $\mathbf{U}^* = (U_i^*)_{i=1,\dots,m}$ used during Stage 3 may contain errors. In this scenario, we define the *noise voltage vector* $\tilde{\mathbf{U}}^* = (\tilde{U}_i^*)_{i=1,\dots,m}$ by

$$\tilde{U}_i^* = U_i^* + \eta \max_{j=1,\dots,m} |U_j^*| \xi_i, \quad i = 1, \dots, m,$$

where $\xi_i \in (-1, 1)$ is obtained using a random normal distribution, and $\eta > 0$ is the noise level. The noise voltage vector $\tilde{\mathbf{U}}^*$ is used during Stage 3, and the gradient method algorithm is applied. Figure 11(a) shows the relative error $\mathrm{RE}(\sigma_\eta, \sigma_{250})$ for a sample of increasing values of noise level parameter η, where σ_{250} is the obtained noiseless conductivity map (see Figure 6(b)). Figure 11(b) shows the contour plot of the conductivity map $\sigma_{abs}(x) = |\sigma_\eta(x) - \sigma_{250}(x)|$, for the particular case $\eta = 0.25$.

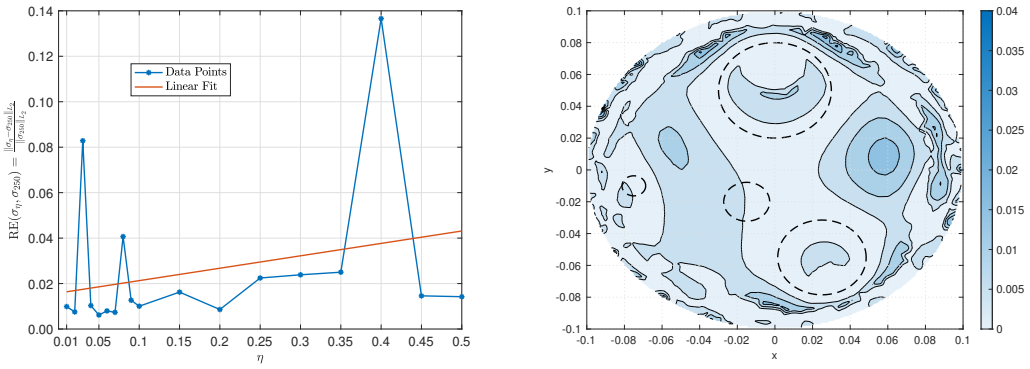

(a) Relative error. **(b)** σ_{abs}

Figure 11. Noise effect for the 4-tumors case in 2D.

4.3. Results in 3D

In this case, we set Q to be the cylinder of radius $r = 0.1$ m and height $h = 0.2$ m, namely

$$Q = \{(x, y, z) \in \mathbb{R}^3 : \ x^2 + y^2 < r^2, \quad 0 < z < h\}. \tag{4.9}$$

A set of $m = 64$ electrodes with dimension 0.024 rad width and 0.012m height were arranged in 4 layers placed in the lateral boundary of Q, see Figure 12(a). These layers are numbered 1 through 4, from the bottom to the top of the cylinder. Figure 12(b) shows the linear mesh domain Q, consisting of 9392 nodes and 49058 elements (tetrahedra) with max (edge) size 0.01. A uniform contact impedance vector $\mathbf{Z} = (Z_l)_{l=1,\dots,m}$ with $Z_l = 0.1$ Ohm was set. Background conductivity is set to 0.2 $(\text{Ohm} \cdot m)^{-1}$ corresponding to healthy tissue, and we assume that the conductivity of cancerous tissue is twice as high. Current pattern vector $\mathbf{I}$ is set by replicating the pattern displayed in Figure 12(c) for each layer of 16 electrodes.

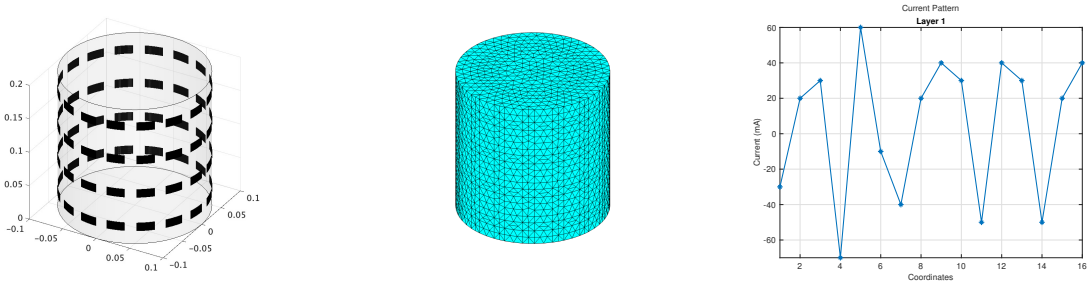

(a) Domain Q. **(b)** Mesh. **(c)** Current.

Figure 12. 3D representation of the cylindrical domain Q displaying electrode size and position (a), and the mesh (b). On the right, (c) current pattern on the first layer of electrodes.

As in the previous section, we will use the following notation for the relative error of voltage and conductivity, respectively.

$$\text{RE}(\mathbf{U}^1, \mathbf{U}^2) = \frac{|\mathbf{U}^1 - \mathbf{U}^2|}{|\mathbf{U}^2|}; \quad \text{RE}(\sigma_1, \sigma_2) = \frac{\|\sigma_1 - \sigma_2\|_{L_2}}{\|\sigma_2\|_{L_2}}.$$

For the optimization process using the GPM algorithm, we set initial conductivity map $\sigma_{ini} = 0.3$ (Ohm $\cdot$ m)$^{-1}$ and initial voltage vector $\mathbf{U}^{ini} = (U_l^{ini})_{l=1}^m$ to $U_l^{ini} = 1$ volt if l is even and $U_l^{ini} = -1$ volt if l is odd. Additionally, we set termination conditions to a maximum number of iterations N_{max} or the relative error tolerance $\epsilon_{tol} = 10^{-6}$. Finally, for all the cases listed below, we define $Q_\varepsilon = \{(x, y, z) \in Q : x^2 + y^2 < (0.1 - \varepsilon)^2\}$ where $\varepsilon > 0$ is given.

4.3.1. Case: 1 tumor

Let us consider $\sigma_{true} : Q \to \mathbb{R}$ determining the spherical tumor with center $c = (0, 0.05, 0.1)$ and radius $r = 0.03$. Figure 13 shows a 3D representation of the conductivity σ_{true}, its position and size within Q, and the corresponding cross-section $x = 0$.

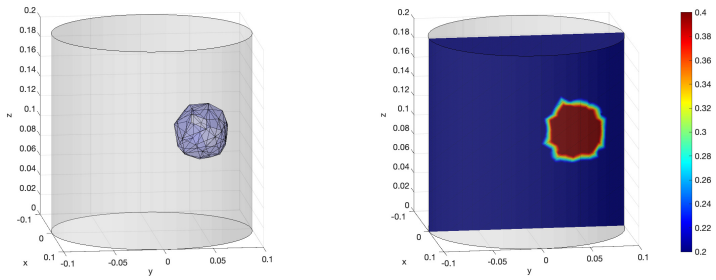

(a) **(b)**

Figure 13. (a) 3D representation of the true conductivity tumor showing its size and location. (b) Contour plot of the cross-section $x = 0$.

The optimal control framework is implemented without regularization ($\beta = 0$). Figure 14 shows 3D reconstruction of σ_{250} for Stage 3 in the region $\{\mathbf{x} \in Q_\varepsilon : \sigma_{250}(\mathbf{x}) > 0.37\}$, for $\varepsilon = 10^{-2}$, and the corresponding contour plot of the cross-section $x = 0$.

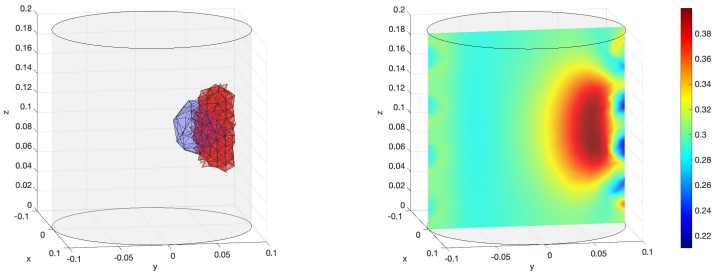

(a) **(b)**

Figure 14. (a) 3D representation of obtained conductivity σ_{250} in the region Q_ϵ. (b) Contour plot of the cross-section $x = 0$ of σ_{250} for Stage 3.

Figure 15(a–c) shows the contour plot of the cross-section $z = 0.1$ (vertical center of Q) of the true conductivity map σ_{true} and calculated conductivity σ_{end} at the last iteration for Stages 2 and 3, respectively. Dashed lines correspond to the position of the true conductivity σ_{true}. Figure 15(d) shows the coordinates $l = 1, \ldots, 16$ (first layer of electrodes) of the obtained voltage vector $\mathbf{U}^{end}$ for Stage 3

in the 1 tumor case. The voltage values at the remaining electrodes match those for the first layer ($l = 1, \ldots, 16$). Cost value at the final iteration $N = 250$ of Stage 3 is $\mathcal{K}(\sigma_{250}, \mathbf{U}^{250}) =$ 7.7029e-08 and relative errors of voltage and conductivity are $\mathrm{RE}(\mathbf{U}^{250}, \mathbf{U}^*) = 0.0696$ and $\mathrm{RE}(\sigma_{250}, \sigma_{true}) = 0.4875$, respectively. In addition, the corresponding tumor resolution error is $\mathrm{TRE}(\sigma_{250}) =$ 2.5899e-04 and the percentage of accuracy in the tumor region is $\mathrm{PAT}(\sigma_{250}) = 83.73\%$. In the case of Stage 2, the corresponding values are $\mathcal{K}(\sigma_{12}, \mathbf{U}^{12}) =$ 1.6000e-03, $\mathrm{RE}(\mathbf{U}^{12}, \mathbf{U}^*) = 0.0905$, $\mathrm{RE}(\sigma_{12}, \sigma_{true}) = 0.5588$, $\mathrm{TRE}(\sigma_{12}) =$ 7.8348e-04 and $\mathrm{PAT}(\sigma_{12}) = 50.80\%$.

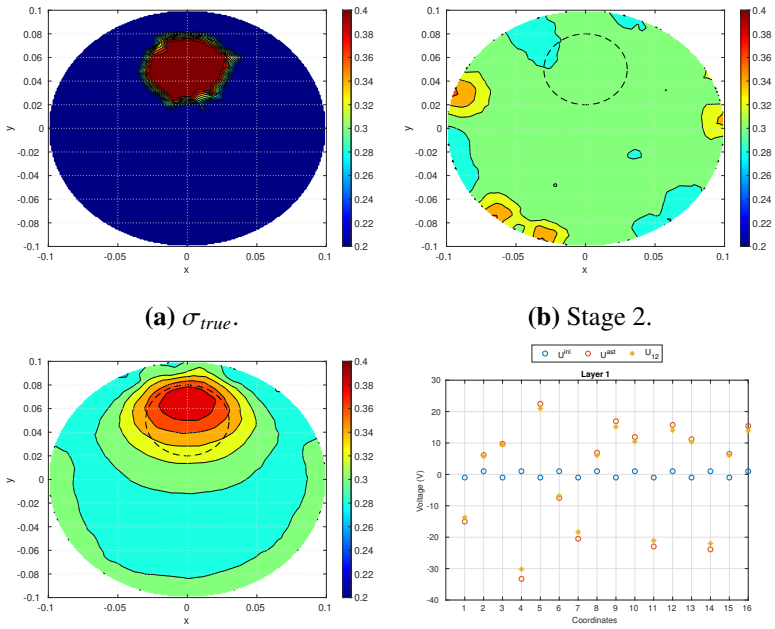

(a) σ_{true}. **(b)** Stage 2.

(c) Stage 3. **(d)** Voltage.

Figure 15. Contour plot of the cross-section $z = 0.1$ of the true conductivity σ_{true} (a), and obtained conductivities σ_{end} at the last iteration for Stages 2 (b) and 3 (c). (d) Coordinates U_l^{end} of the obtained voltage after Stage 3.

Sensitivity with respect to size. For this analysis, we have considered σ_{true} for fixed center $c = (0, 0.05, 0.1)$ and three different values of radius r between 0.03 and 0.01. Figure 16 shows the cross-section $z = 0.1$ of the reconstructed conductivity σ_N and the last iteration $N = 250$ for the cases $r = 0.025, 0.020, 0.015$. Dashed lines show the location and size of σ_{true}. Table 4 shows the values of the cost functional and relative error with respect to voltage and conductivity at the last iteration of Stage 3 for each case of radius r.

Sensitivity with respect to location. Let us consider σ_{true} with fixed radius $r = 0.03$ and different center positions, namely $c = (0, 0.05, 0.1)$, $(0, 0.03, 0.1)$, $(0, 0.01, 0.1)$. Figure 17 shows the cross-section contour plot at $z = 0.1$ of obtained conductivity for the cases $c = (0, c_y, 0.1)$, with $c_y = 0.04, 0.03, 0.02$. Table 5 shows the corresponding cost functional values and relative error with respect to voltage and conductivity at the final iteration of Stage 3 for each case of center c.

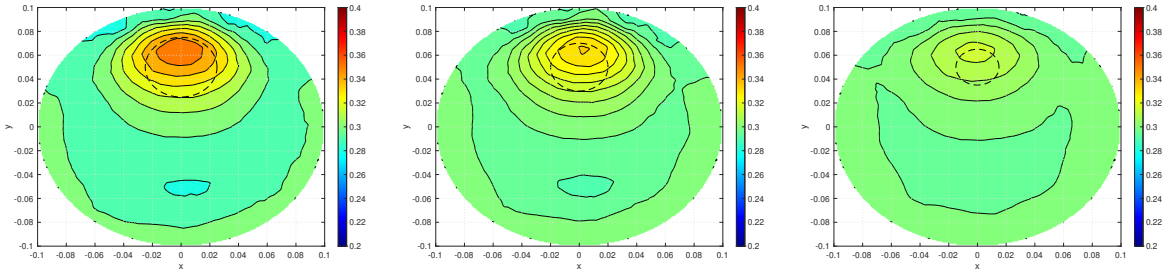

(a) $r = 0.025$ **(b)** $r = 0.020$ **(c)** $r = 0.015$

Figure 16. Contour plot of the cross-section $z = 0.1$ of obtained conductivity σ_{250} for different values of radius r for σ_{true}.

Table 4. Metrics for the 3D - Case 1 tumor - Size.

Radius	Cost value	Relative error		TRE(σ_{end})	PAT(σ_{end})
(r)	$\mathcal{K}(\sigma_{end}, \mathbf{U}^{end})$	RE($\mathbf{U}^{end}, \mathbf{U}^*$)	RE($\sigma_{end}, \sigma_{true}$)		
0.030	7.7029e-08	0.0697	0.4876	2.5899e-04	83.73%
0.025	2.7787e-08	0.0698	0.4884	3.1539e-04	71.90%
0.020	1.2547e-08	0.0699	0.4974	2.7066e-04	64.17%
0.015	3.6822e-09	0.0700	0.5008	1.6213e-04	56.96%
0.010	2.1157e-09	0.0700	0.5023	5.5463e-05	52.37%

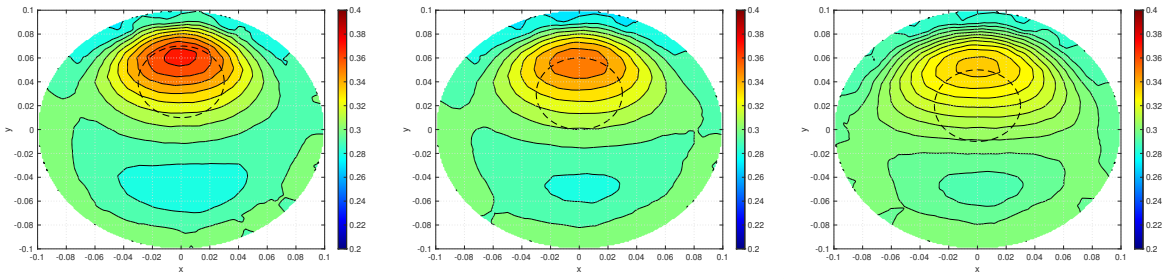

(a) $c = (0, 0.04, 0.1)$ **(b)** $c = (0, 0.03, 0.1)$ **(c)** $c = (0, 0.02, 0.1)$

Figure 17. Contour plot of the cross-section $z = 0.1$ of obtained conductivity σ_{250} for different values of center c for σ_{true}.

Table 5. Metrics for the 3D - Case 1 tumor - Location.

Center	Cost Value	Relative Error		TRE(σ_{end})	PAT(σ_{end})
(c_y)	$\mathcal{K}(\sigma_{end}, \mathbf{U}^{end})$	RE($\mathbf{U}^{end}, \mathbf{U}^*$)	RE($\sigma_{end}, \sigma_{true}$)		
0.05	7.7029e-08	0.0697	0.4876	2.5899e-04	83.73%
0.04	6.5934e-07	0.0697	0.4895	4.3140e-04	73.75%
0.03	2.9617e-08	0.0698	0.4850	5.3145e-04	66.77%
0.02	2.5079e-08	0.0698	0.4862	6.4927e-04	59.75%
0.01	2.0786e-08	0.0698	0.4870	7.2406e-04	55.09%
0.00	1.9150e-08	0.0698	0.4869	7.3625e-04	54.23%

4.3.2. Case: 2 tumors

In this section, we consider $\sigma_{true} : Q \to \mathbb{R}$ determining two spherical tumors with center $c_1 = (0, 0.05, 0.1)$, $c_2 = (0, -0.05, 0.1)$ and radius $r_1 = r_2 = 0.03$. Figures 18 show the 3D representation of σ_{true} and the vertical cross-section $x = 0$.

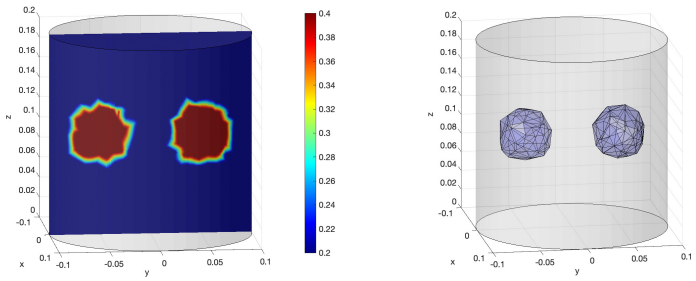

(a) 3D representation. **(b)** Cross-section $x = 0$.

Figure 18. 3D plots of the true conductivity σ_{true} in the 2 tumors case.

Figure 19 shows the horizontal cross-section $z = 0.1$ (center of the cylinder) of the true conductivity σ_{true}, and the obtained conductivities σ_{end} at the last iteration for Stages 2 and 3, respectively.

Figure 20 shows the reconstruction of calculated conductivity σ_{171} for Stage 3 in the region $\{\mathbf{x} \in Q_\varepsilon : \sigma_{171}(\mathbf{x}) > 0.37\}$, for $\varepsilon = 10^{-2}$, and the cross-sections $x = 0$ of σ_{171}. Finally, the cost value at the last iteration of Stage 3 is $\mathcal{K}(\sigma_{171}, \mathbf{U}^{171}) = 7.7029\text{e-}08$ and corresponding relative errors for voltage and conductivity are, respectively, $\mathrm{RE}(\mathbf{U}^{171}, \mathbf{U}^*) = 0.0683$ and $\mathrm{RE}(\sigma_{171}, \sigma_{true}) = 0.4527$. In addition, the tumor resolution error is $\mathrm{TRE}(\sigma_{171}) = 3.6900\text{e-}04$ and the percentage of accuracy in the tumor region is $\mathrm{PAT}(\sigma_{171}) = 83.81\%$.

Remark 4.3. Notice that, by comparing the conductivity map for the 1-tumor case (see Figure 15(c)) and the corresponding conductivity for the 2-tumor case (see Figure 19(c)), the results indicate that the addition of an extra tumor of the same size does not affect the optimization process, preserving the resolution of the reconstructed conductivity map of the target tumorous region.

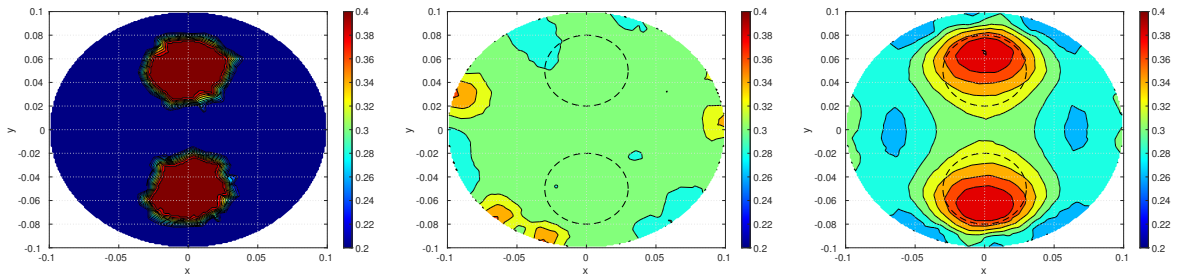

(a) σ_{true}. **(b)** Stage 2. **(c)** Stage 3.

Figure 19. Cross-section $z = 0.1$ of σ_{true} and calculated σ_{end} at the last iteration of Stages 2 and 3.

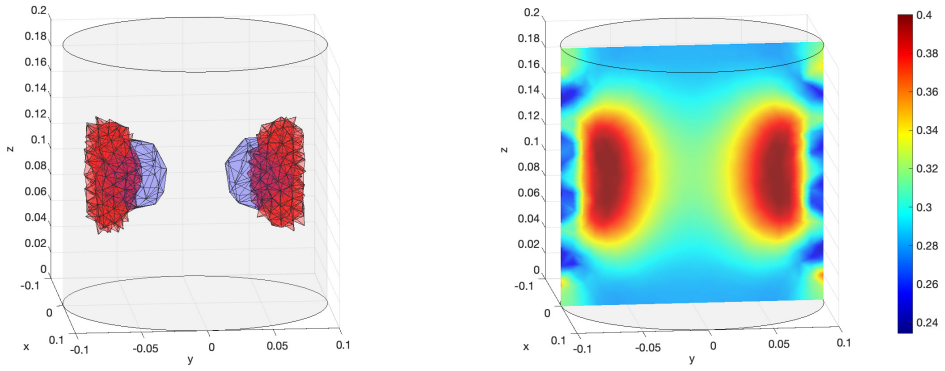

(a) **(b)**

Figure 20. 3D representation of obtained conductivity σ_{250} in the region Q_ϵ, and corresponding ontour plot of the cross-section $x = 0$ for Stage 3.

Sensitivity with respect to size. In this case, we consider the scenario in which the size of one of the tumors, as determined by the initial true conductivity σ_{true}, is reduced. Indeed, we set $r_2 = 0.015$, positions c_1, c_2 and radius r_1 are kept the same. The obtained new conductivity will be denoted $\tilde{\sigma}_{true}$. The optimal control framework is implemented without regularization ($\beta = 0$). Figure 21 show the 3D representation of $\tilde{\sigma}_{true}$, and corresponding cross-sections $x = 0$.

Figure 22 shows cross-sections $x = 0$ of the true conductivity σ_{true}, and obtained conductivities σ_{20} and σ_{138} for Stages 2 and 3, respectively. Dashed lines show the position and size of true conductivity $\tilde{\sigma}_{true}$. Figure 23 shows the reconstruction of calculated conductivity σ_{138} at the last iteration for Stage 3 in the region $\{\mathbf{x} \in Q_\varepsilon : \sigma_{138}(\mathbf{x}) > 0.35\}$, for $\varepsilon = 10^{-2}$, as well as the cross-section $x = 0$.

Sensitivity with respect to location. In this case, we consider the scenario in which the center of the tumors, as determined by the initial true conductivity σ_{true}, is modified. Indeed, we set $c_1 = (0, 0.05, 0.05)$, $c_2 = (0, -0.05, 0.15)$, the radius $r_1 = r_2 = 0.03$ are preserved. The new conductivity will be denoted $\bar{\sigma}_{true}$. Figure 24 show the 3D representation of $\bar{\sigma}_{true}$ and cross-section $x = 0$, respectively.

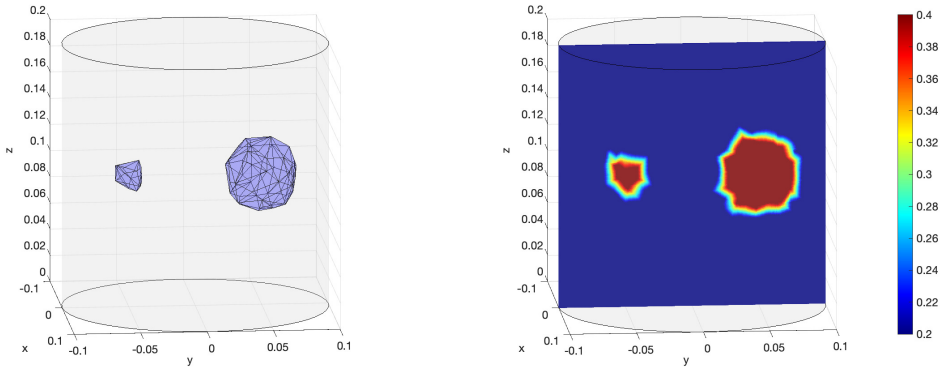

(a) **(b)**

Figure 21. 3D representation of the true conductivity σ_{true} and the corresponding cross-section $x = 0$.

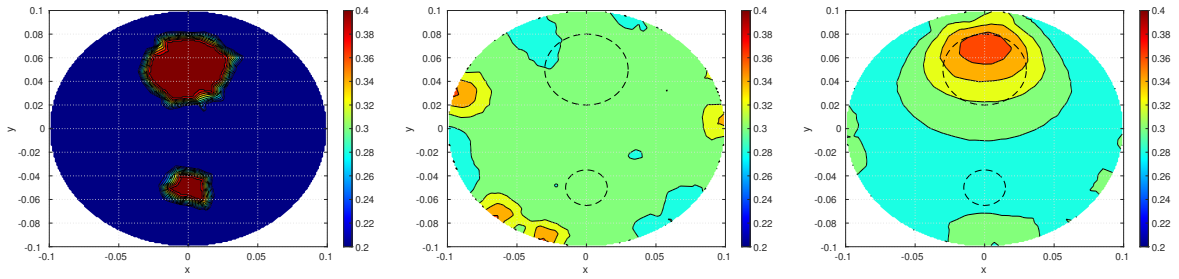

(a) $\tilde{\sigma}_{true}$. **(b)** Stage 2. **(c)** Stage 3.

Figure 22. Contour plot of the cross-section $x = 0$ of true and obtained conductivities on each Stage.

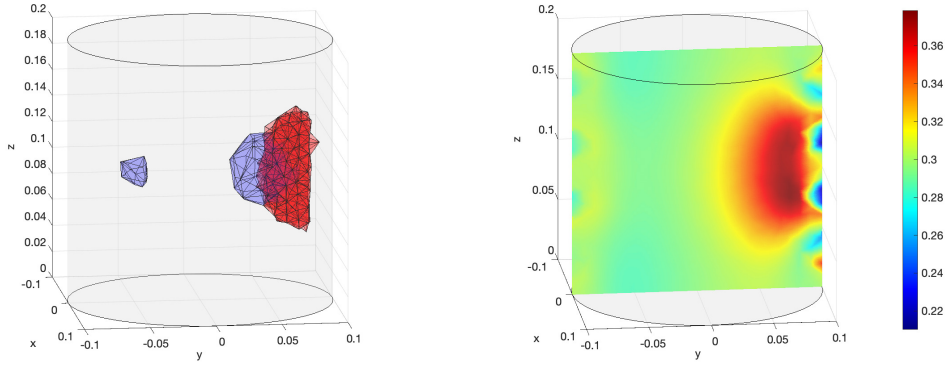

(a) **(b)**

Figure 23. 3D representation of the obtained conductivity σ_{138} in the region Q_ε for Stage 3, and the corresponding contour plot of the cross-section $x = 0$.

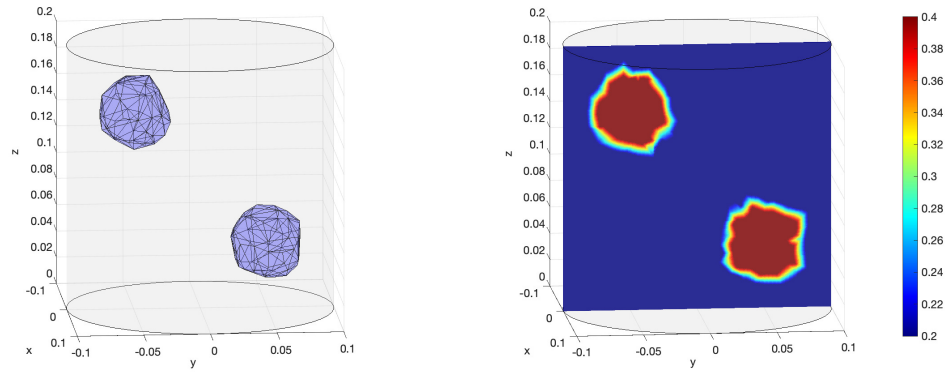

(a) **(b)**

Figure 24. 3D representation of the true conductivity σ_{true} , and the corresponding contour plot of the cross-section $x = 0$.

The optimal control framework is implemented without regularization ($\beta = 0$). Figure 25 shows the

contourplot of the cross-sections $z = 0.05$ and $z = 0.15$, through the center of each tumor, of the true conductivity $\bar{\sigma}_{true}$ and the reconstructed conductivities σ_{20} and σ_{180} for Stages 2 and 3, respectively.

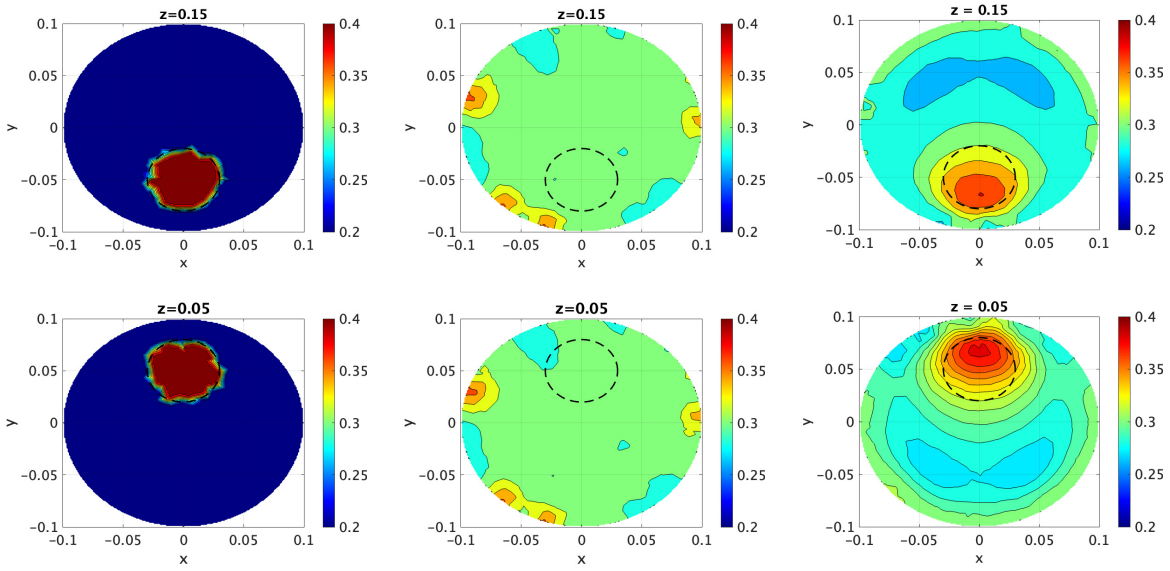

(a) $\bar{\sigma}_{true}$. **(b)** Stage 2. **(c)** Stage 3.

Figure 25. Contour plot of the cross-section $z = 0.05$ and $z = 0.15$ of the true conductivity $\bar{\sigma}_{true}$, and obtained conductivities at each Stage.

Finally, Figure 26 shows the 3D representation the cross-section $x = 0$ of the obtained conductivity σ_{180} for Stage 3 at the last iteration in the region $\{\mathbf{x} \in Q_\varepsilon : \sigma_{180}(\mathbf{x}) > 0.35\}$, for $\varepsilon = 10^{-2}$.

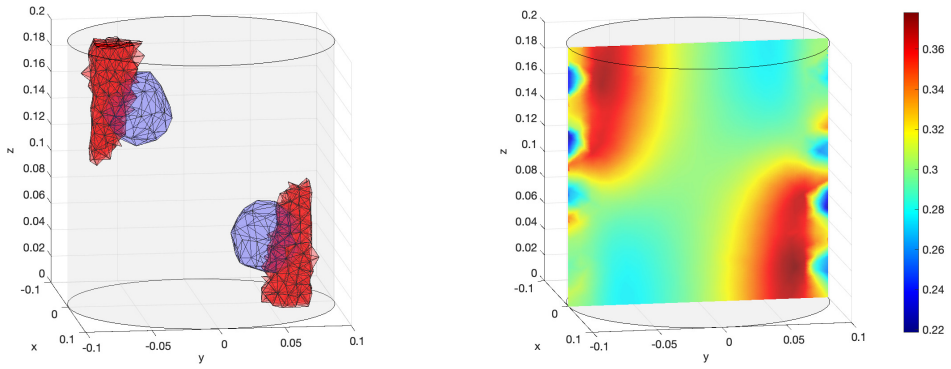

(a) **(b)**

Figure 26. 3D portion reconstruction of the obtained conductivity σ_{180} in the region Q_ε, and corresponding cross-section $x = 0$.

4.3.3. Case: 4 tumors

In this section, we consider the case of σ_{true} determining four spherical tumors of center $c_1 = (0, 0.05, 0.1)$, $c_2 = (-0.075, -0.01, 0.1)$, $c_3 = (-0.015, -0.02, 0.1)$, $c_4 = (0.025, -0.055, 0.1)$, and

respective radius $r_4 = 0.03$, $r_2 = 0.0099$, $r_3 = 0.15$ and $r_4 = 0.02$. The optimal control framework is first implemented without regularization ($\beta = 0$) and the results obtained at Stages 2 and 3 are displayed in Figure 27. Figure 28 shows 3D representation of σ_{true} and reconstructed conductivity σ_{250} within the region $\{\mathbf{x} \in Q_\varepsilon : \sigma_{250}(\mathbf{x}) > 0.35\}$, for $\varepsilon = 10^{-2}$, respectively.

Regarding Stage 3, the cost functional value at the last iteration $N = 250$ is $\mathcal{K}(\sigma_{250}, \mathbf{U}^{250}) =$ 6.7785e-05, and the relative error of voltage and conductivity is $\mathrm{RE}(\mathbf{U}^{250}, \mathbf{U}^*) = 0.0693$ and $\mathrm{RE}(\sigma_{250}, \sigma_{true}) = 0.4659$. Additionally, the tumore resolution error is $\mathrm{TRE}(\sigma_{250}) =$ 4.7220e-04 and the percentage of accuracy in the tumor region is $\mathrm{PAT}(\sigma_{250}) = 75.09\%$.

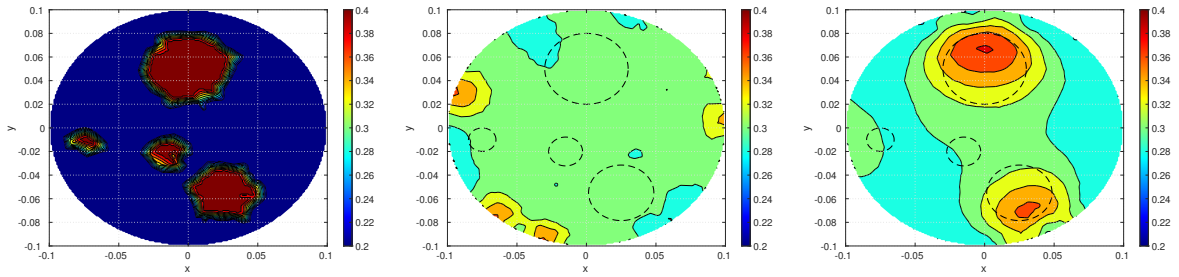

(a) σ_{true}. **(b)** Stage 2. **(c)** Stage 3.

Figure 27. Contour plot of the cross-section $z = 0.1$ of the true conductivity σ_{true} and obtained conductivities at the last iteration for each Stage.

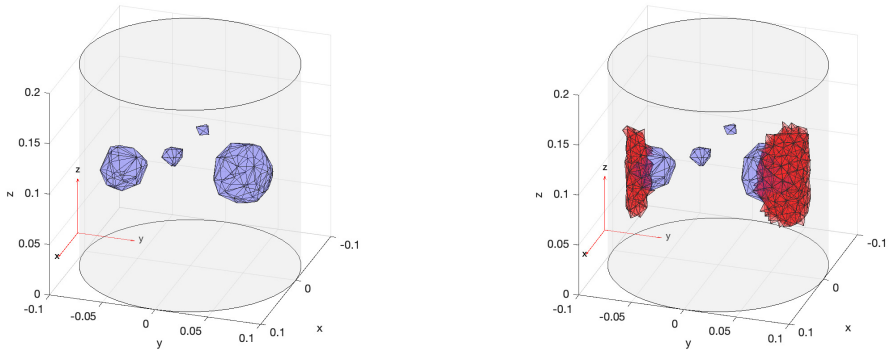

(a) **(b)**

Figure 28. 3D representation of the true conductivity σ_{true} and portion reconstruction of the obtained conductivity σ_{250} in the region Q_ε.

Sensitivity with respect to size. Here we considered different values for the tumor cell with center c_2 and radius r_2 of σ_{true}. Indeed, the radius r_2 is increased while the center c_2 is recalculated to preserve the distance to the lateral boundary of Q. Figure 29 shows the cross-section $z = 0.1$ (center of the cylinder) of σ_{end} for all the cases of radius r_2. Figure 30 shows 3D reconstruction of the region $\{\mathbf{x} \in Q_\varepsilon : \sigma_{250}(\mathbf{x}) > 0.35\}$, for $\varepsilon = 10^{-2}$. Table 6 shows the cost value and relative errors of voltage and conductivity at the last iteration of Stage 3 and for each case radius r_2.

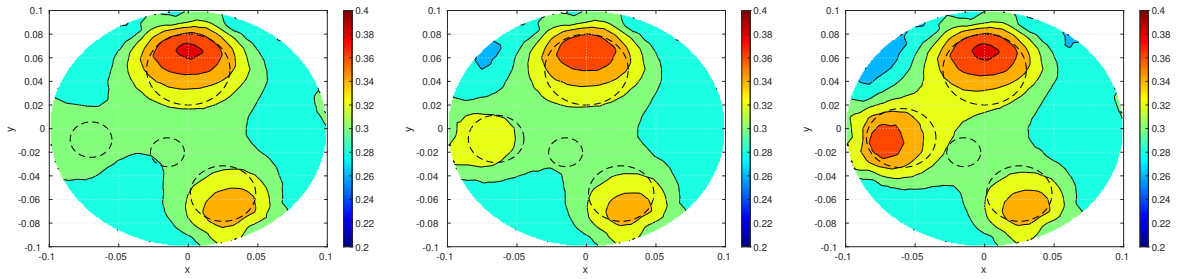

(a) $r_2 = 0.015$. **(b)** $r_2 = 0.020$. **(c)** $r_2 = 0.025$.

Figure 29. Contour plot of the cross-section $z = 0.1$ of the obtained conductivity σ_{250} after Stage 3 for different values of the radius r_2.

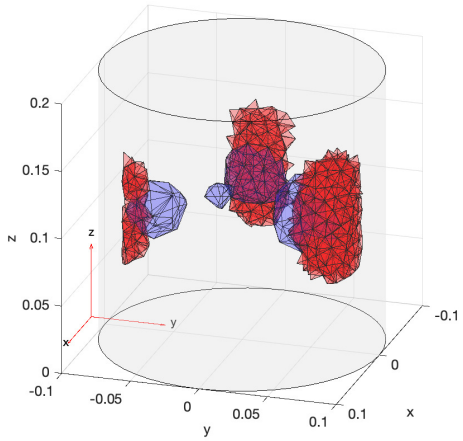

Figure 30. 3D portion reconstruction of σ_{250} in the region Q_ε for the case $r_2 = 0.025$.

Table 6. Metrics for the 3D - Case 4 tumors - Size.

Radius	Cost value	Relative error		TRE(σ_{end})	PAT(σ_{end})
(r_2)	$\mathcal{K}(\sigma_{end}, \mathbf{U}^{end})$	RE($\mathbf{U}^{end}, \mathbf{U}^*$)	RE($\sigma_{end}, \sigma_{true}$)		
0.015	9.3826e-08	0.0693	0.4703	4.9061e-04	74.51%
0.020	1.0858e-07	0.0691	0.4632	5.6185e-04	72.19%
0.025	8.8688e-08	0.0692	0.4600	5.3311e-04	75.97%

Regularization effect. We consider here the effect of regularization in the reconstruction/optimization process. Initial conditions σ_{ini} and $\mathbf{U}^{ini}$ were set to those obtained after 250 iterations in Stage 3 without regularization (see Figure 27(c)). Figure 31 shows the cross-section contour plot of the resulting conductivity (with values in $(\text{Ohm} \cdot \text{m})^{-1}$) for different values of the regularization parameter β. Table 7 shows the cost value and relative errors of voltage and conductivity at the last iteration. The minimum value of the cost functional, and relative error of control parameters are minimized at the value 10^{-3} of the regularization parameter. Precisely, the minimum value of the cost functional is reduced from order 10^{-5} to 10^{-8}, while the resolution error of the conductivity is reduced from 47% to

9%. Improved cost functional minimum and resolution error as a result of regularization, the resolution of the reconstructed optimal conductivity is refined. Comparing Figure 31(b) to Figure 27(c), we see that the resolution of the reconstructed conductivity recognizes the smaller size tumor as an effect of regularization.

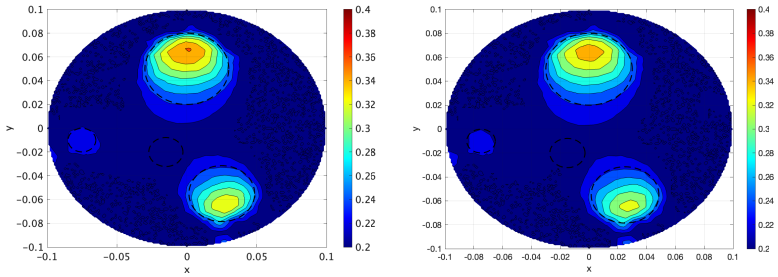

(a) σ_{500}; β = 1e-02. **(b)** σ_{527}; β = 1e-03.

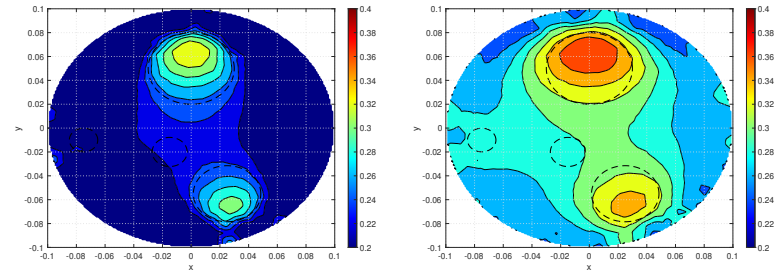

(c) σ_{1000}; β = 1e-05. **(d)** σ_{1000}; β = 1e-06.

Figure 31. Contour-plot of the cross-section $z = 0.1$ for the obtained conductivity σ_{end} during Stage 3 for different values of regularization parameter β.

Table 7. Metrics for the 3D - Case 4 tumors - Regularization.

Param.	Cost value	Relative error		TRE(σ_{end})	PAT(σ_{end})
(β)	$\mathcal{K}(\sigma_{end}, \mathbf{U}^{end})$	RE($\mathbf{U}^{end}, \mathbf{U}^*$)	RE($\sigma_{end}, \sigma_{true}$)		
1e-02	8.9280e-08	1.5836e-06	0.0981	9.6275e-04	49.22%
1e-03	4.2204e-08	9.3427e-06	0.0910	1.0076e-03	46.85%
1e-05	1.7765e-07	9.0933e-04	0.1027	1.0299e-03	45.67%
1e-06	6.9503e-06	0.0191	0.3554	5.0295e-04	73.47%

Noise effect. Like in the 2D case, we consider here the scenario in which the measured voltage $\mathbf{U}^*$ used during Stage 3 may contain errors. The noise voltage vector $\tilde{\mathbf{U}}^* = (\tilde{U}_i^*)_{i=1,\dots,m}$ is given by

$$\tilde{U}_i^* = U_i^* + \eta \max_{j=1,\dots,m} |U_j^*| \xi_i, \quad i = 1, \dots, m,$$

where $\xi_i \in (-1, 1)$ is obtained using a random normal distribution and $\eta > 0$ is the noise level. The voltage $\tilde{\mathbf{U}}^*$ is used during Stage 3, and the gradient method algorithm is applied. Figure 32(a) shows the relative error RE($\sigma_\eta, \sigma_{250}$) for a sample of increasing values of noise level parameter η, where σ_{250} is the noiseless optimized conductivity map (see Figure 27(c)). Figure 32(b) shows the contour

plot of the cross-section $z = 0.1$ of the corresponding pointwise absolute difference conductivity map $\sigma_{abs} = |\sigma_{\eta_1} - \sigma_{250}|$ for the particular case $\eta = 0.10$.

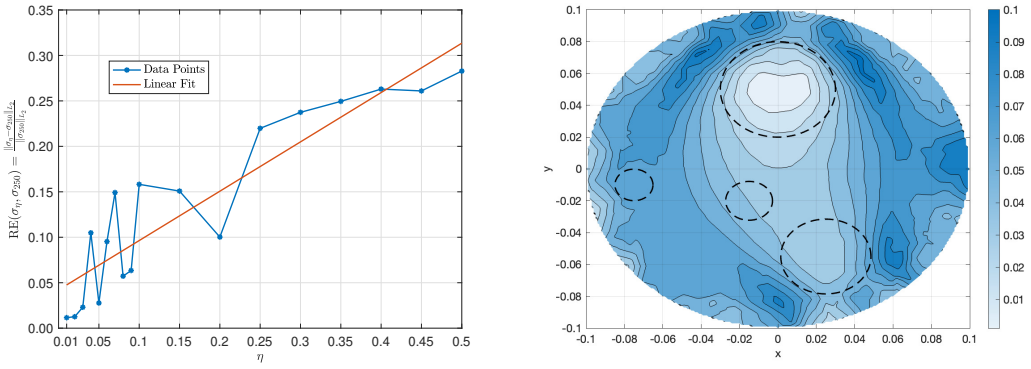

(a) Relative error. **(b)** σ_{abs}

Figure 32. Noise effect for the 4-tumors case in 3D.

Remark 4.4. The sensitivity analysis shows that the reconstruction of the target conductivity map improves with the size of the tumorous region and its proximity to the boundary electrodes. It is worth noting that a finer mesh can improve the precision and accuracy of the target region measurement.

Remark 4.5. It is worth noting that numerical simulations in 3D are substantially more expensive than those in 2D. Indeed, by performing the computations on an iMac desktop computer equipped with an Apple M1 chip and 8GB of memory, an iteration during Stage 3 for the 3D case can take approximately 90 seconds, whereas 3 seconds for the 2D case. The increase in computational cost in the 3D case is explained not only by the larger number of finite elements considered for the mesh, but also by the larger number of electrodes, which corresponds to a larger number of differential equations to be solved during an iteration. Finally, it is expected that the larger number of finite elements and nodes in the 3D model requires a larger amount of memory to perform the average number of iterations, in which case most desktop computers may not be used. For this reason, all calculations in the 3D case were performed using the cluster provided by the Core Facilities at the institution (OIST).

Remark 4.6. The adoption of a cylindrical domain is motivated by practical medical applications in which the body segment of interest (breast) is placed within a cup of comparable geometry, while two-dimensional circular domains serve as cross-sectional representations of the corresponding cylinder. Moreover, such geometries are relatively straightforward to implement numerically. Nevertheless, EIT models have also been applied to applications involving the gastrointestinal tract, lung cancer, and brain activity, which may necessitate more complex geometries and fully three-dimensional modeling techniques or specialized software [13]. Finally, it is important to notice that the theoretical results presented in Section 3 do not depend on the shape of the domain.

5. Discussion

We consider an inverse EIT problem on the identification of the conductivity map in the complete electrode model based on the m current-to-voltage measurements on the boundary electrodes.

Particular motivation arises from the medical application for the identification of the cancerous tumor at early stages of development. The idea of the method is based on the fact that the electrical conductivity of the cancerous tumor is significantly higher than the conductivity of the healthy tissue. A variational formulation as a PDE-constrained optimal control problem is introduced based on the novel idea of increasing the size of the input data by adding "voltage-to-current" measurements through various permutations of the single "current-to-voltage" measurement. The idea of permutation preserves the size of the unknown parameters at the expense of increasing the number of PDE constraints. We apply a Gradient Projection Method based on the Fréchet differentiability in Besov-Hilbert spaces.

- Numerical simulations demonstrate that for both 2D and 3D model examples, the resolution of target tumor regions is significantly improved by increasing the number of input data from m to m^2.

- Resolution of target tumor regions is demonstrated to be sensitive to the size of the tumor and its distance from the boundary electrodes. Smaller tumor size and greater distance from the electrodes negatively impact the resolution of tumors produced by the method. A combination of the GPM algorithm with the regularization method significantly improves the resolution to recognize smaller tumors.

- Based on the effective computational performance, a new 2-step procedure is suggested for the medical application for the identification of the cancerous tumor at an early stage of its development.

The advantages of EIT procedures are twofold. First, they require relatively simple instrumentation and are therefore significantly more cost-effective, particularly when compared with advanced imaging modalities such as MRI, which is rarely used as a primary screening tool [13]. Second, EIT techniques are minimally invasive and do not subject patients to repeated or cumulative radiation exposure, as is the case with x–ray–based methods. The cumulative x-ray exposure itself poses a risk, and the procedure can cause significant discomfort, which may discourage patients from submitting to regular examinations [13].

6. Conclusions

This paper suggests a new method for the identification of cancerous tumors at an early stage of development. Relying on the experimental fact that the electrical conductivity of the cancerous tumor is significantly higher than the conductivity of the healthy tissue, we consider an inverse EIT problem on the identification of the conductivity map in the complete electrode model based on the m current-to-voltage measurements on the boundary electrodes. A variational formulation as a PDE-constrained optimal control problem is introduced. To address the ill-posedness of the inverse problem due to insufficient measurements, we implement a novel idea of increasing the size of the input data by adding "voltage-to-current" measurements through various permutations of the single "current-to-voltage" measurement. The idea of permutation preserves the size of the unknown parameters at the expense of an increase in the number of PDE constraints. We apply a gradient projection method based on the Fréchet differentiability in Besov-Hilbert spaces. Numerical simulations of 2D and 3D model examples demonstrate the sharp increase in the resolution of the cancerous tumor by increasing the

number of measurements from m to m^2. Based on the effective computational performance, a new 2-step procedure is suggested for the identification of the cancerous tumor at an early stage of its development in the clinical setting.

Author contributions

UGA initiated the idea of the new method, pursued all the mathematical proofs and rigorous analysis, and supervised the project; JHR pursued coding and software development for the numerical implementation of the new method; UGA and JHR pursued validation and computational analysis of numerical simulations; UGA drafted the manuscript; Both UGA and JHR read and agreed with the final version of the manuscript.

Use of Generative-AI tools declaration

The authors declare that they have not use Artificial Intelligence (AI) tools in the creation of this article.

Acknowledgements

The authors are grateful for the help and support provided by the Scientific Computing and Data Analysis section of the Core Facilities at OIST.

Availability of data and materials

The datasets generated and/or analysed during the current study are not publicly available due to potential conflicts with other research groups, but are available from the corresponding author on reasonable request.

Conflict of interest

All authors declare they have no competing interests.

References

1. U. G. Abdulla, V. Bukshtynov, S. Seif, Cancer detection through Electrical Impedance Tomography and optimal control theory: theoretical and computational analysis, *Math. Biosci. Eng.*, **18** (2021), 4834–4859. https://doi.org/10.3934/mbe.2021246
2. U. G. Abdulla, S. Seif, Discretization and convergence of the eit optimal control problem in sobolev spaces with dominating mixed smoothness, *Contemp. Math.*, **784** (2023). https://doi.org/10.1090/conm/784/15750
3. G. S. Alberti, H. Ammari, B. Jin, J. K. Seo, W. Zhang, The linearized inverse problem in multifrequency electrical impedance tomography, *SIAM J. Imaging Sci.*, **9** (2016), 1525–1551. https://doi.org/10.1137/16M1061564

4. M. Alsaker, J. L. Mueller, A D-bar algorithm with a priori information for 2-dimensional electrical impedance tomography, *SIAM J. Imaging Sci.*, **9** (2016), 1619–1654. https://doi.org/10.1137/15M1020137

5. H. Ammari, H. Kang, *Reconstruction of small inhomogeneities from boundary measurements*, Lecture Notes in Mathematics, Vol. 1846, Springer, 2004. https://doi.org/10.1007/b98245

6. J. Barzilai, J. M. Borwein, Two-point step size gradient methods, *IMA J. Numer. Anal.*, **8** (1988), 141–148. https://doi.org/10.1093/imanum/8.1.141

7. R. S. Blue, D. Isaacson, J. C. Newell, Real-time three-dimensional electrical impedance imaging, *Physiol. Meas.*, **21** (2000), 15. https://doi.org/10.1088/0967-3334/21/1/303

8. A. P. Calderón, On an inverse boundary value problem, *Seminar on Numerical Analysis and Its Application to Continuum Physics, Brazilian Mathematical Society (SBM)*, 1980, 65–73.

9. M. Dodd, J. L. Mueller, A real-time D-bar algorithm for 2-D electrical impedance tomography data, *Inverse Probl. Imaging*, **8** (2014), 1013–1031. https://doi.org/10.3934/ipi.2014.8.1013

10. M. Gehre, B. Jin, X. Lu, An analysis of finite element approximation in electrical impedance tomography, *Inverse Probl.*, **30** (2014), 045013. https://doi.org/10.1088/0266-5611/30/4/045013

11. R. J. Halter, T. Zhou, P. M. Meaney, A. Hartov, R. J. B. Jr, K. M. Rosenkranz, et al., The correlation of *in vivo* and *ex vivo* tissue dielectric properties to validate electromagnetic breast imaging: initial clinical experience, *Physiol. Meas.*, **30** (2009), S121. https://doi.org/10.1088/0967-3334/30/6/S08

12. S. J. Hamilton, J. M. R. S. Siltanen, X. Zhang, A hybrid segmentation and D-bar method for electrical impedance tomography, *SIAM J. Imaging Sci.*, **9** (2016), 770–793. https://doi.org/10.1137/15M1025992

13. D. S. Holder, *Electrical impedance tomography: methods, history and applications*, 1 Ed., CRC Press, 2005. https://doi.org/10.1201/9780367801595

14. N. Hyvönen, L. Päivärinta, J. P. Tamminen, Enhancing D-bar reconstructions for electrical impedance tomography with conformal maps, *Inverse Probl. Imaging*, **12** (2018), 373–400. https://doi.org/10.3934/ipi.2018017

15. B. Jin, Y. Xu, J. Zou, A convergent adaptive finite element method for electrical impedance tomography, *IMA J. Numer. Anal.*, **37** (2017), 1520–1550. https://doi.org/10.1093/imanum/drw045

16. C. E. Kenig, J. Sjöstrand, G. Uhlmann, The Calderón problem with partial data, *Ann. Math.*, **165** (2007), 567–591. https://doi.org/10.4007/annals.2007.165.567

17. F. Kleinermann, N. J. Avis, S. K. Judah, D. C. Barber, Three-dimensional image reconstruction for electrical impedance tomography, *Physiol. Meas.*, **17** (1996), A77. https://doi.org/10.1088/0967-3334/17/4A/011

18. K. Knudsen, M. Lassas, J. L. Mueller, S. Siltanen, Reconstructions of piecewise constant conductivities by the D-bar method for electrical impedance tomography, *J. Phys.: Conf. Ser.*, **124** (2008), 012029. https://doi.org/10.1088/1742-6596/124/1/012029

19. O. Kwon, J. K. Seo, J. R. Yoon, A real-time algorithm for the location search of discontinuous conductivities with one measurement, *Commun. Pure Appl. Math.*, **55** (2002), 1–29. https://doi.org/10.1002/cpa.3009

20. S. Laufer, A. Ivorra, V. E. Reuter, B. Rubinsky, S. B. Solomon, Electrical impedance characterization of normal and cancerous human hepatic tissue, *Physiol. Meas.*, **30** (2010), 995–1009. https://doi.org/10.1088/0967-3334/31/7/009

21. A. I. Nachman, Reconstructions from boundary measurements, *Ann. Math.*, **128** (1988), 531–576. https://doi.org/10.2307/1971435

22. A. I. Nachman, Global uniqueness for a two-dimensional inverse boundary value problem, *Ann. Math.*, **142** (1995), 71–96. https://doi.org/10.2307/2118653

23. J. K. Seo, E. J. Woo, Magnetic resonance electrical impedance tomography (MREIT), *SIAM Rev.*, **53** (2011), 40–68. https://doi.org/10.1137/080742932

24. S. Siltanen, J. Mueller, D. Isaacson, An implementation of the reconstruction algorithm of A Nachman for the 2D inverse conductivity problem, *Inverse Probl.*, **17** (2001), 1561. https://doi.org/10.1088/0266-5611/17/5/501

25. E. Somersalo, M. Cheney, D. Isaacson, Existence and uniqueness for electrode models for electric current computed tomography, *SIAM J. Appl. Math.*, **52** (1992), 1023–1040. https://doi.org/10.1137/0152060

26. J. Sylvester, G. Uhlman, A global uniqueness theorem for an inverse boundary value problem, *Ann. Math.*, **125** (1987), 153–169. https://doi.org/10.2307/1971291

27. T. Widlak, O. Scherzer, Hybrid tomography for conductivity imaging, *Inverse Probl.*, **28** (2012), 084008. https://doi.org/10.1088/0266-5611/28/8/084008

AIMS Press